University of Leoben

Dissertation

Structural Investigation of Size Effects in Plasticity using Indentation Techniques

Martin Rester

Leoben, April 2008

This work was financially supported by the Austrian Science Fund (FWF) through project P 17375-N07.

Erich Schmid Institute of Materials Science
Austrian Academy of Sciences
Jahnstrasse 12
A–8700 Leoben

This thesis was typeset by the use of KOMA-Script and LaTeX 2ε.

To my family

Affidavit

I declare in lieu and oath, that I wrote this thesis and performed the associated research myself, using only literature cited in this volume.

Leoben, April 2008

Acknowledgements

I would like to express my gratitude to a number of persons who have contributed and supported me during course of this work. I, particularly, wish to thank:

- Reinhard Pippan, my supervisor, for his guidance and support and for giving an expertise to this thesis.
- Christian Motz, my co-supervisor, for his support and help and the patience especially during the early stages of my work.
- Gerhard Dehm, the head of the department of materials physics for giving me the opportunity to work here.
- My office colleagues, former office colleagues and “non-office” colleagues, Peter Gruber, Megan Cordill, Martin Hafok, Gerhard Jessner, Stefan Massl, Klaus Martinschitz, Daniel Kiener and Hans-Peter Wörgöter for their help, countless discussions and a lot of fun.
- Thomas Schöberl for his skilled help when it comes to nanoindentation and Jörg Thomas for support with the TEM.
- Edeltraud Haberz for the excellent sample preparation and Franz Hubner for the fabrication of various apparatuses.
- All employees of the Erich Schmid Institute for their help.
- My family and friends for their support and friendship.

Abstract

It was found, that contrary to the predictions of classic continuum plasticity theory, the plastically deformed zone below nano-, micro- and macroindentations is not self-similar. Rather, different stages of deformation associated with varying sizes of the deformed regions were detected.

Examining cross-sections through nanoindentations in copper by means of electron backscatter diffraction (EBSD) technique, show that different characteristic deformation patterns occur. For large nanoindentations (2.5 mN–10 mN) a plastically deformed zone, which consists of three characteristic regions is found, while for shallow nanoindentations ($\leq$ 1 mN) only two characteristic sections appear. Due to these findings it can be assumed, that a change in the deformation mechanism between large and shallow nanoindentations takes place. Analysis of the corresponding hardness data in terms of geometrically necessary dislocations (GNDs) using the Nix-Gao model, supports the assumption of a "mechanism change". To explain the observed behavior, two models based on possible dislocation arrangements are suggested and compared to the experimental findings. The model presented for large imprints is similar to the dislocation pile-up model explaining the Hall-Petch effect, while the model for shallow nanoindentations uses far-reaching dislocation loops to accommodate the shape change caused by the indenter. Further evidence for a change of the deformation mechanism were delivered by additionally performed transmission electron microscopy (TEM) experiments. As the TEM experiments show, the plastically deformed zone of large nanoindents consists of high density dislocation networks, intermitted by almost dislocation free regions. The deformation zone found for small nanoindentations, however, looks somewhat different. Instead of dense networks of dislocations, the plastically deformed zone is built up by single dislocation loops surrounding the imprint.

The plastic deformation zone below microindentations ($>$ 10 mN–300 mN) can as well be divided into three characteristic regions. Noticeable is, that the dimension of the zone where significant changes of the orientation occur, is proportional to the size of the imprint.

For macroindentations ($>$ 300 mN–100 N) the plastically deformed zone consists of only two characteristic regions. The identified regions exhibit a structure, which is typical for low and medium deformed face-centered cubic single crystals of pure metals. With increasing load, dislocation substructures which exhibit orientation fluctuations in the micron regime, occur.

Summarizing the microstructural results of all examined indentations it becomes apparent, that the size of the indentations cover a wide range of the different scales of structural evolution, appearing during the deformation of a single crystal. It seems that the hardness of a material varies with the size of indentation, as the flow stress of a single crystal with the evolving substructure.

Istud, quod tu summum putas,
gradus est

What you think is the summit,
is only a step up

Lucius Annaeus Seneca (4 AC–65 AD)

Contents

1

Introduction

1.1 A short review on indentation size effect

Indentation testing is perhaps one of the most common methods to characterize the mechanical properties of a material. In such a test, a hard tip of spherical or pyramidal shape is pressed under a fixed load into the material.[1] The hardness is then expressed as the ratio of the load to the imprint area. The first widely accepted and standardized hardness test was a technique proposed by Brinell in 1900, where a hard steel ball is used as indenter.[2] Using the Brinell hardness test, Meyer[3] performed a series of investigations and found that the hardness of a material is not load-independent. For a given ball diameter of the indenter, he expressed the following empirical relationship:

$$P = ad^n \tag{1.1}$$

Here P is the load, a and n are constants of the material under examination and d is the diameter of the residual impression. Plotting P versus d in a logarithmic diagram results in curves which are straight lines, of which the slope is numerically equal to the so-called Meyer index n. This method of determining n is known as "Meyer analysis" and has been used as a test for the hardness-load dependence. An n-value less than 2 indicates an increase of hardness with decreasing load, whereas for an n-value larger than 2, the hardness decreases with decreasing load. If the Meyer index equals 2, there is proportionality between load and imprint area, and the hardness is load-independent. However, it was found that the value of n is typically unequal 2, indicating a load-dependency of the hardness.

An explanation for the observed behavior was delivered by Tabor,[4] who attributed the appearing load-dependence to the fact that ball indenters do not produce geometrically similar imprints, since the angle between imprint flank and sample surface changes with the depth of penetration. One type of indenter, which meets this geometric similarity, is the Vickers indenter.[5,6] Consequently, Meyer analysis of Vickers hardness data should yield a constant Meyer index of 2. In the following many studies were performed using the Vickers hardness test and it was found that the Vickers hardness as well is load-dependent, especially at low loads.[6–9]

In the following, great efforts were made to explain the observed behavior. Generally, two sets of explanations can be distinguished. The first set concerns experimental errors,[10] resulting from the resolution of the objective lens,[11,12] the geometry of the indenter,[13] friction between indenter and specimen[13–15] and errors associated with sample preparation.[7,8,16,17] The second set[1,18] is directly related to the intrinsic structural factors of the tested materials, including e.g. indentation elastic recovery[14,19–25] and work hardening during indentation.[1] The conclusion was, that load-dependent hardness is a genuine effect and is not caused by instrumental errors or the presence of a surface layer. A more detailed review on the early work of load-dependent hardness can be found in the work of Mott.[1]

One of the first systematic investigations on load-dependency of hardness, was performed by Upit and Varchenya[26–29] on various single crystalline materials, using a low-load microhardness testing device. Upit and Varchenya found that the increase in hardness with decreasing load, is associated with a corresponding reduction of the size of dislocation assemblies, surrounding the indentations. They called the observed variation of hardness with load, “size effect”. However, the term “indentation size effect” (ISE) was accepted years later. At the same time, Gane and Cox[30,31] performed indentation experiments on single crystalline gold. Gane and Cox found, that hardness could be increased by a factor of three when decreasing the contact diameter down to 200 nm. They suggested, that the increase must have some fundamental origins, connected to dislocation processes occurring in the stressed volume around the indenter.

More than one decade later, the development of instrumented nanoindentation techniques rekindled the interest in the phenomenon of load-dependent hardness. Instrumented indentation technique was used by Pethica et al.[32] to perform hardness tests on nickel, gold and silicon using indenter penetration depths as low as 20 nm. The indenter penetration was monitored continuously during loading and unloading, while the areas of the indents were determined by means of a scanning electron microscope (SEM).[33] For every material under examination a pronounced indentation size effect was found, especially for depths less than 100 nm. Pethica et al. explained the indentation size effect by local extreme work hardening, since all glide planes are active and intersecting in regions less than 100 nm across.[32]

Further improvement of instrumented nanoindentation technique was achieved by the work of Doerner and Nix[34] as well as Oliver and Pharr.[35] The enhanced technique made the determination of mechanical properties from load-displacement curves possible, even when the indentations were too small to be imaged conveniently. Driven by the growing interest in the deformation of small material volumes caused by the development of thin films and the increased use of nanostructured materials, load and displacement sensing indentation became a major tool to investigate the mechanical properties of materials. Many authors used this by now economical and routine method, and as a consequence research in this field continuously increased.

To account for the size dependency of strength, Fleck and Hutchinson[36] introduced a new plasticity law, the so-called strain gradient plasticity (SGP) theory. Founded on the concept of geometrically necessary dislocations (GNDs),[37–40] the SGP theory incorporates a material length scale and thus can describe many size effects in plastically deforming metals.[41,42] Fleck et al.[41] have pointed out, that the indentation size effect for metals can be understood by noting that large strain gradients inherent in small indentations lead to GNDs that cause enhanced hardening.[43] The same physical description was given earlier by Stelmashenko et al.[44] and De Guzman et al.[45] to explain the phenomenon of depth-dependent hardness, however, connections to strain gradient plasticity theory were not made.[43] Ma and Clarke,[46] who investigated size dependent hardness of silver single crystals, used an identical physical description and finally recognized its connection to SGP theory.[43] A more detailed review on strain gradient plasticity theory can be found in.[47–50]

Using the concept of geometrically necessary dislocations, Nix and Gao[43] suggested a mechanism-based ISE model. Since the so-called Nix-Gao model is the most cited description in order to explain the ISE, in the following a detailed overview of the model is given. Nix and Gao considered, that indentation is done by a rigid cone which is accommodated by circular loops of GNDs with Burgers vectors normal to the plane of the surface. Assuming that the injected loops are stored in a hemisphere under the contact perimeter, the GND-density becomes

$$\rho_G = \frac{3}{2bh} tan^2\theta \tag{1.2}$$

where b is the Burgers vector, h is the depth of indentation and θ is the apex half-angle of the indenter. Dislocations which are created additionally to GNDs by other nucleation processes, and those which were already present in the material prior to indentation, are called statistically stored dislocations (SSDs).[39] Using the Taylor relation,[51,52] the deformation resistance can be estimated as follows:

$$\tau = \alpha\mu b\sqrt{\rho_G + \rho_S} \tag{1.3}$$

where α is a constant, μ is the shear modulus and ρ_S is the density of SSDs. Assuming that the von Mises flow rule[54] and Tabors rule[53] apply, the following expression can be found:

$$\frac{H}{H_0} = \sqrt{1 + \frac{h^*}{h}} \tag{1.4}$$

where

$$H_0 = 3\sqrt{3}\alpha\mu b\sqrt{\rho_S} \tag{1.5}$$

is the hardness that would arise from the statistically stored dislocations alone, and

$$h^* = \frac{81}{2} b\alpha^2 tan^2\theta \left(\frac{\mu}{H_0}\right)^2 \tag{1.6}$$

is a length that characterizes the depth dependence of the hardness. As can be seen, the indentation size effect can be predicted by Eq. 1.4. For large penetration depths, the ratio h^*/h is negligible and the hardness is equal to H_0, while in cases, where the indentation depth h is of the same order of magnitude as h^*, the indentation size effect is included. It can be seen from Eq. 1.4, that a linear relationship between H^2 and $1/h$ exists, which agrees well with the microindentation hardness data obtained by McElhaney et al.[55] and Ma and Clarke.[46]

However, as many experiments showed, nanoindentation data do not follow this linear trend over the whole measurement range.[56–59] Especially at small indentation depths, the hardness data start to deviate from the predicted linear curve. To account for the observed non-linear behavior, many authors modified the conventional Nix-Gao model using different approaches like incorporating the effect of intrinsic lattice resistance,[60] varying the GND-density or the GND-storage volume[50, 58, 59, 61–64] or taking into account the indenter tip roundness.[65, 66] The most prominent of the aforementioned approaches is those which deals with an expansion of the GND-storage volume, and as a consequence several efforts have been made to quantify the plastically deformed volume.[67–70] The results of the accomplished experiments, which are mainly transmission electron microscopy (TEM) plane views through the indented area, confirm that the plastically deformed zone expands far beyond the suggested hemispherical volume. The appearance of far-propagating dislocations is also corroborated by in-situ TEM nanoindentation experiments,[71] as well as by numerous computer simulations.[72–76]

1.2 Aim of the present work

The aim of the current work is to better understand, how the size of the plastically deformed volume influences the resistance of a material against plastic deformation. This is important, since the successful design of nano-composites, micro-electro-mechanical system (MEMS) devices, thin films, optoelectronic devices or the development of high strength nano-structured materials, depends on the knowledge of basic deformation mechanisms, operating at small scales. From the macroscopic point of view, the deformation behavior of materials can be described by continuum plasticity models. However, discrete dislocation processes inside the material are ignored in such models. Consequently, when decreasing the size of the deformed volume, the discrete nature of plasticity has to be considered. This is necessary, since local mechanical properties are directly linked to the deformation structure at this level. To get insight into the deformation behavior of the material at the microscale, indentation techniques were used to study basic deformation mechanisms in small volumes, as well as how strain gradients, obstacles (e.g. grain boundaries), etc., influences these mechanisms. Special attention was paid, to explain the observed effects by the use of simple metal physical concepts.

1.3 Summary of the thesis

In order to investigate the deformation mechanisms responsible for size effects in indentation experiments, several cross-sections through nanoindentations in copper $\{111\}$ single crystals were fabricated by means of focused ion beam (FIB) technique (see paper A). The indentations, with loads between 500 μN and 10 mN, were produced using a Hysitron TriboScope, fitted with a cube corner indenter. On the readily polished cross-sections, electron backscatter diffraction (EBSD) investigations were performed, to get quantitative information about the appearing microstructure and the occurring deformation mechanisms. For large nanoindentations, i.e. 10, 5 and 2.5 mN, respectively, a deformation zone consisting of three distinct regions which exhibit significant crystal orientation changes was found. The plastically deformed volume of indentations produced at smaller loads ($\leq$ 1 mN), on the other hand, consists of only two characteristic regions. Comparing the deformation zones found for large and for small nanoindentations show that they are not self-similar. Furthermore, the plastically deformed volume relatively increases, as the indentation depth decreases.

Differences between large and shallow nanoindentations were also found in the misorientation profiles across the indenter flank. For large imprints a misorientation plateau close to the indenter flank appears, followed by an exponential decrease of the misorientation towards the undeformed crystal. The misorientation profile for shallow nanoindentations exhibits no misorientation plateau. However, starting directly at the indenter flank, the misorientation decreases exponentially.

Considering the experimental findings it can be assumed that a change of the deformation mechanism between large and shallow imprints occurs. To check this assumption, the determined hardness data were analyzed using Nix-Gao plots, where the square of the hardness is plotted versus the reciprocal indentation depth. Contrary to the predicted linear trend a bi-linear relationship with different slopes for large and for shallow nanoindentations was found. Like the results obtained from the EBSD experiments, this observation as well indicates a change in the deformation mechanism.

To explain the observed mechanism change, two models based on possible dislocation arrangements are presented and compared to the experimental findings. For large indentations, a dislocation pile-up model similar to those used to explain the Hall-Petch (H-P) effect is suggested, while in the model for shallow imprints far-reaching dislocation loops accommodate the shape change caused by the indenter. Comparing the models to the experimental findings, show very good agreement. The dislocation model describing large imprints accommodates the shape of the indentation and explains the observed crystal orientation changes, and those proposed for shallow nanoindentations reflects the observed only slight orientation changes in an excellent manner.

Since both suggested models are associated with mechanisms that are based on the pile-up* of dislocations, the hardness data were also plotted in terms of the Hall-Petch relation. It was found that the regime for large nanoindentations as well as those for shallow ones show a linear trend in the Hall-Petch plot too. Due to this finding, it would appear that pile-up based deformation mechanisms are responsible for the accommodation of large and shallow imprints.

To confirm the appearance of a deformation change as well as to find evidence which support the proposed dislocation models, TEM investigations of the plastically deformed volume are of great interest. Thus, cross-sectional TEM samples through nanoindentations made at loads of 10 mN and 0.5 mN, respectively, were fabricated (see paper B)†. For the high load indentation, a deformed volume consisting of highly confined deformation-induced patterns was found. The TEM analysis of the indentation made at 0.5 mN, however, exhibited deformation patterns which are ambiguous. Instead of a dense dislocation network, which encloses the large indentation, the small indentation is surrounded by only few dislocation loops. Additionally performed selected area electron diffraction (SAED) shows large orientation gradients beneath the deep imprint, and only small gradients near the shallow indentation. It is assumed that the plastic zone of small nanoindentations consists of dislocation loops, which propagate far into the bulk material and induce the observed only slight misorientation gradient. This observation is in contrast to one of the basic predictions of the Nix-Gao model, that especially for very small indentations a high strain gradient occurs. As a consequence, the following question is raised: "Where are the geometrically necessary dislocations at small indentations?"

To answer the question, the deformation zones below nanoindentations performed in the vicinity of a twin boundary, were investigated (see paper C). Since it is assumed, that GNDs required to realize the permanent shape change of the surface propagate far into the bulk, introducing a barrier should result in a dislocation pile-up and as a consequence in increased misorientation and hardness values. A twin boundary of known orientation was used as well defined dislocation obstacle. EBSD examinations of the plastically deformed volume exhibited regions of increased misorientation in front of the boundary. Comparing the found deformation zone to the deformation zone found beneath an imprint in a copper single crystal, confirms that the twin boundary stops the otherwise far-propagating dislocations. Similar results were found in additionally performed TEM experiments. As the TEM micrograph of a 0.5 mN imprint shows, a very dense dislocation network between imprint tip and twin boundary appears. However, the regions besides the dislocation network are almost dislocation-free. Since the piled-up dislocations produce a large back

---

* In addition to the classical understanding, in this work the term "pile-up" also refers to an arrangement of dislocations in a "pile-up"-like structure, where the back-stress is produced by expanding dislocation loops pushed into the bulk.

† Additional information on the preparation of TEM samples using the in-situ lift-out method and low energy FIB milling can be found in paper G.

stress which impedes subsequent dislocation generation, the hardness in the vicinity of the twin boundary should be increased. In order to check this assumption, the dependence of the hardness on the distance to the twin boundary, was measured. It was found that the hardness increases significantly as the distance to the boundary is decreased. This fact further indicates that small indentations are accommodated by a mechanism which is based on the pile-up of dislocations.

The suggested dislocation models are supported by many of the experimental findings. However, an analytical treatment of the dislocation arrangements in order to check if they are realistic, is as well of great interest. Thus, in paper D, the shear stress required to obtain the proposed dislocation arrangements is estimated. Since the model describing the indentation process of large imprints shows similarity to the Hall-Petch effect, the H-P relation is used for shear stress calculation. For shallow imprints, on the other hand, the required shear stress can not be estimated in this way. Due to the fact that single dislocation events are very important for the accommodation of small imprints, the dislocation source size as well as the back stress originating from previous emitted dislocations are considered for stress calculation. Using Tabors rule the calculated stresses were converted into hardness values and compared to the measured hardness. Although the performed estimations are only rough, very good agreement between calculated and measured hardness was found.

Up to now, all of the mentioned experiments were performed on copper crystals. However, it is well known that dislocation patterns, formed during plastic deformation, are dependent on the stacking fault energy (SFE). Thus, metals with differing SFE might show different dislocation arrangements. As a consequence, the plastically deformed volume below indentations made in various metals, should be different. In order to check this assumption, EBSD investigations of cross-sections through nanoindentations in silver, copper and nickel, were performed (see paper E). Comparison of the obtained misorientation maps of the various metals showed that no significant differences between the plastically deformed zones exist. Since the occurring dislocation arrangements are directly linked to the hardness of a metal, in addition the impact of the SFE on the ISE of the different metals was examined. For this purpose, nanoindentations with loads between 40 μN and 10 mN were made. Plotting the obtained hardness data in a conventional hardness versus indentation depth (H vs. h) plot showed no considerable effect of the SFE on the ISE. Even though the hardness of all three metals differs significantly, the general H vs. h behavior is very similar. To normalize the hardness curves, the reduced indentation modulus was identified to be the most suitable parameter. Comparison of the normalized hardness curves exhibited, that the curves are almost on top of each other. Due to these observations, as well as the results obtained from EBSD studies it become apparent that the SFE do not influence the ISE, not even at small indentation depths. This fact further supports the assumption that for small imprints the dislocation source stress as well as the back stress of dislocations are the most important parameters controlling the hardness of a metal.

In the aforementioned experiments, the plastically deformed volume below nanoindentations made with loads between 0.5 mN and 10 mN, were investigated. But what happens to the microstructure, if the applied load and consequently the indentation depth is further increased? This question is addressed in paper F, where by means of EBSD technique the plastically deformed zones of imprints up to loads of 100 N are investigated. Analysis of the EBSD misorientation maps shows that three characteristic “microstructural” regimes can be distinguished. Regime α, where the imprints are smaller than 200 nm, is characterized by deformation patterns showing only slight misorientation changes. In regime β, where the indentations are between 200 nm and 10 μm in depth, the microstructure exhibits distinctive changes of the orientation. In this regime the dimension of the misorientation patterns is proportional to the size of the indentation. Moreover, the orientation differences increase with growing indentation depth, especially between 200 nm and 1 μm. Regime γ, on the other hand, associated with indentations larger than 10 μm, is indicated by a substructure which typically forms during the plastic deformation of face-centered cubic single crystals of pure metals. Plotting the corresponding hardness data in a logarithmic diagram shows that the “microstructural” regimes are reflected in the hardness curve, too.

Analysis of the appearing microstructure showed, that the size of the indents covers a wide range of the different scales of structural evolution occurring during the deformation of a single crystal. Due to the differences in the developed dislocation substructure it is not surprising that hardness changes with the size of indentation. It seems that the hardness of the material varies with the size of indentation, as the flow stress of a single crystal with the evolving substructure. It has to be noticed that the finest substructure forms at small imprints and the substructure size increases as the indentation depth is increased. Only for very shallow imprints the source size becomes important and has to be considered additionally.

Bibliography

[1] Mott BW. Micro-Indentation Hardness Testing. London: Butterworths Publications Ltd.; 1956.

[2] Brinell JA. Mémoire sur les épreuves à bille en acier. In: Communications présents devant le congrès international des méthodes d'essai des matériaux de construction, Tome 2. Paris: 1901. p.83.

[3] Meyer E. Z Ver Dtsch Ing 1908;52:648.

[4] Tabor D. Sheet Metal Ind 1954;31:749.

[5] Kick F. Z Österr Ing Arch Ver 1890;42:1.

[6] Onitsch EM. Berg Hüttenmänn Mh 1948;93:7.

[7] Schulz F, Hanemann H. Z Metallkd 1941;33:124.

[8] Bernhardt EO. Z Metallkd 1941;33:135.

[9] Mitsche R. Österr Chem Z 1948;49:186.

[10] Bückle H. Z Metallkd 1954;45:623.

[11] Brown ARG, Ineson E. J Iron Steel Inst 1951;169:376.

[12] Bückle IH. Metall Rev 1959;4:49.

[13] Vitovec F. Berg Hüttenmänn Mh 1951;96:133.

[14] Bischof W, Wenderott B. Arch Eisenhüttenw 1941/42;15:497.

[15] Mitsche R, Onitsch EM. Betr Fert 1949;3:157.

[16] Raub E. Mitt Forsch Inst Edelmet 1942:7.

[17] Hill R, Lee EH, Tupper SJ. Proc Roy Soc 1947;188A:273.

[18] Bückle IH. Use of the hardness test to determine other material properties. In: Westbrook JH, Conrad H, editors. The Science of Hardness Testing and its Research Applications. Metals Park (OH): American Society for Metals, 1973. p.453.

[19] Knoop F, Peters CG, Emerson WB. J Res Nat Bur Stand 1939;23:39.

[20] Braun A. Schwz Arch Angew Wiss Tech 1953;19:67.

[21] Braun A. Z Metallkd 1955;46:499.

[22] Schulze R. Feinwerkt 1951;55:190.

[23] Bergsman EB. Amer Soc Test Mat Bull 1951;176:37.

[24] Tate DR. Trans ASM 1945;35:374.

[25] Tarasov LP, Thibault NW. Trans ASM 1947 ;38 :331.

[26] Upit GP, Varchenya SA. Phys Status Solidi 1966;17:831.

[27] Varchenya SA, Muktepavel FO, Upit GP. Phys Status Solidi A 1970;1:K165.

[28] Upit GP, Varchenya SA. The Size Effect on the Hardness of Single Crystals. In : Westbrook JH, Conrad H, editors. The science of hardness testing and its research applications. Metals Park (OH): American Society for Metals, 1974. p.135.

[29] Manika I, Maniks J. Acta Mater 2006;54:2049.

[30] Gane N. Proc Roy Soc A 1970;317:367.

[31] Gane N, Cox JM. Philos Mag 1970;22:881.

[32] Pethica JB, Hutchings R, Oliver WC. Philos Mag A 1983;48:593.

[33] Oliver WC, Hutchings R, Pethica JB. Measurements of hardness at indentation depths as low as 20 nanometers. In: Blau PJ, Lawn BR, editors. Microindentation Techniques in Materials Science and Engineering, Spec. Tech. Publ. 889. Philadelphia: American Society of Testing and Materials, 1986. p.90.

[34] Doerner MF, Nix WD. J Mater Res 1986;1:601.

[35] Oliver WC, Pharr GM. J Mater Res 1992;7:1564.

[36] Fleck NA, Hutchinson JW. J Mech Phys Solids 1993;41:1825.

[37] Nye JF. Acta Metall 1953;1:153.

[38] Cottrell AH. The Mechanical Properties of Matter. New York: Wiley; 1964.

[39] Ashby MF. Philos Mag 1970;21:399.

[40] Ashby MF. The deformation of plastically non-homogeneous alloys. In: Kelly A, Nicholson RB, editors. Strengthening Methods in Crystals. Philadelphia: American Society of Testing and Materials, 1971. p.137.

[41] Fleck NA, Muller GM, Ashby MF, Hutchinson JW. Acta Metall Mater 1994;42:475.

[42] Fleck NA, Hutchinson JW. Adv Appl Mech 1997;33:295.

[43] Nix WD, Gao H. J Mech Phys Solids 1998;46:411.

[44] Stelmashenko NA, Walls MG, Brown LM, MilmanYV. Acta Metall Mater 1993;41:2855.

[45] De Guzman MS, Neubauer G, Flinn P, Nix WD. Mater Res Symp Proc 1993;308:613.

[46] Ma Q, Clarke DR. J Mater Res 1995;10:853.

[47] Gao H, Huang Y, Nix WD, Hutchinson JW. J Mech Phys Solids 1999;47:1239.

[48] Huang Y, Qu S, Hwang KC, Li M, Gao H. Int J Plasticity 2004;20:753.

[49] Abu Al-Rub RK, Voyiadjis GZ. Int J Plasticity 2004;20:1139.

[50] Abu Al-Rub RK. Mech Mater 2007;39:787.

[51] Taylor GI. Proc Roy Soc Lond A 1934;145:362.

[52] Taylor GI. J Inst Met 1938;62:307.

[53] Tabor D. Proc R Soc A 1947;192:247.

[54] von Mises R. Z Angew Math Mech 1928;8:161.

[55] McElhaney KW, Vlassak JJ, Nix WD. J Mater Res 1998;13:1300.

[56] Lim YY, Chaudhri YY. Philos Mag A 1999;79:2979.

[57] Elmustafa AA, Stone DS. Acta Mater 2002;50:3641.

[58] Swadener JG, George EP, Pharr GM. J Mech Phys Solids 2002;50:681.

[59] Feng G, Nix WD. Scripta Mater 2004;51:599.

[60] Qiu X, Huang Y, Nix WD, Hwang KC, Gao H. Acta Mater 2001;49:3949.

[61] Durst K, Backes B, Göken M. Scripta Mater 2005;52:1093.

[62] Huang Y, Zhang F, Hwang KC, Nix WD, Pharr GM, Feng G. J Mech Phys Solids 2006;54:1668.

[63] Durst K, Backes B, Franke O, Göken M. Acta Mater 2006;54:2547.

[64] Durst K, Franke O, Böhner A, Göken M. Acta Mater 2007;55:6825.

[65] Qu S, Huang Y, Nix WD, Jiang H, Zhang F, Hwang KC. J Mater Res 2004;19:3423.

[66] Alkorta J, Martínez-Esnaola JM, Gil Sevillano J. Acta Mater 2006;54:3445.

[67] Chiu YL, Ngan AHW. Acta Mater 2002;50:2677.

[68] Patriarche G, Le Bourhis E, Faurie D, Renault PO. Thin Solid Films 2004;460:150.

[69] Wo PC, Ngan AHW, Chiu YL. Scipta Mater 2006;55:557.

[70] Wo PC, Ngan AHW, Chiu YL. Scipta Mater 2007;56:323.

[71] Minor AM, Asif SAS, Shan Z, Stach EA, Cyrankowski E, Wyrobek TJ, Warren OL, Nature Mater 2006;5:697.

[72] Kelchner CL, Plimpton SJ, Hamilton JC, Phys Rev B 1998;58:11085.

[73] Li J, Van Vliet KJ, Zhu T, Yip S, Suresh S, Nature 2002;418:307.

[74] Balint DS, Deshpande VS, Needleman A, Van der Giessen E, J Mech Phys Solids 2006;54:2281.

[75] Kreuzer HGM, Pippan R, Acta Mater 2007;55:3229.

[76] Nicola L, Bower AF, Kim KS, Needleman A, Van der Giessen E, J Mech Phys Solids 2007;55:1120.

2

List of appended papers

Paper A
M. Rester, C. Motz and R. Pippan
Microstructural investigation of the volume beneath nanoindentations in copper
Acta Materialia 55 (2007) 6427

Paper B
M. Rester, C. Motz and R. Pippan
The deformation-induced zone below large and shallow nanoindentations – A comparative study using EBSD and TEM
Submitted for publication in Philosophical Magazine Letters

Paper C
M. Rester, C. Motz and R. Pippan
Where are the geometrically necessary dislocations at small indentations?
Manuscript under preparation

Paper D
M. Rester, C. Motz and R. Pippan
Microstructural investigation of the deformation zone below nano-indents in copper
Materials Research Society Symposium Proceeding 1049 (2007) AA03-03

Paper E
M. Rester, C. Motz and R. Pippan
Stacking fault energy and indentation size effect: Do they interact?
Scripta Materialia 58 (2008) 187

Paper F
M. Rester, C. Motz and R. Pippan
Indentation across size scales – A survey of indentation-induced plastic zones in copper {111} single crystals
Accepted for publication in Scripta Materialia

Paper G
M. Rester
TEM sample preparation using the FIB lift-out method and low energy ion milling
Not published

A

Microstructural investigation of the volume beneath nanoindentations in copper

M. Rester, C. Motz and R. Pippan

Erich Schmid Institute of Materials Science, Austrian Academy of Sciences,
A–8700 Leoben, Austria

Abstract

The deformed volume below nanoindentations in copper single crystals with a $\langle 1\bar{1}0\rangle \{111\}$ orientation is investigated. Using a focused ion beam workstation, cross-sections through nanoindentations were fabricated and examined using the electron backscatter diffraction technique. Additionally a transmission electron microscopic foil through the middle of an imprint was prepared and analysed. Due to changes in the crystal orientation around and beneath the indentations the plastically deformed zone can be visualized and compared with the measured hardness values. Furthermore, the hardness data were analysed in terms of geometrically necessary dislocations using the Nix-Gao model, where a linear relationship was found for H^2 vs. $1/h_c$, but with different slopes for large and shallow indentations. The orientation "micrographs" indicate that this behavior is associated with a change in the deformation mechanism. Consequently, two models based on possible dislocation arrangements are presented and compared with the experimental findings. For large indentations a dislocation pile-up model similar to those used to explain the Hall-Petch effect is suggested, while the model for shallow imprints uses far-reaching dislocation loops to accommodate the shape change of the indenter.

A.1 Introduction

The characterization of the deformation zone below indentations has been an area of active investigation in order to improve the understanding of the mechanisms occurring during indentation. Early works focused on the visualization of the deformed volume beneath microindentations by means of light microscopy using split samples[1,2] or cleaving indented specimens.[3] In recent years the use of the focused ion beam (FIB) technique has simplified the fabrication of cross-sectional samples and allows a more accurate examination of the deformation zone. Tsui et al.[4] and Inkson et al.[5] used this technique to investigate cross-sections through indentations by means of a scanning electron microscope (SEM). However, implementation of the electron backscatter diffraction (EBSD) technique in SEMs facilitated a more accurate study of the deformed volume below indentations. Zaafarani et al.,[6] for example, used three-dimensional EBSD to investigate the texture and microstructure below a 900 nm deep spherical indentation. Kiener et al.,[7] on the other hand, applied conventional EBSD technique to study the plastically deformed volume below Vickers indentations down to an indentation depth of 700 nm. However, to get information about individual dislocation arrangements associated with the deformation, the use of a transmission electron microscope (TEM) is essential. Most of the accomplished work focused on the investigation of TEM plane views through the indented area.[8–14] Nowadays use of the FIB technique simplifies sample preparation and makes the extraction of site-specific TEM foils feasible.[15–22] A recent development is in situ nanoindentation performed in a TEM, which provides real-time observations of the mechanisms of plastic deformation that occur during indentation.[23,24]

Attempts to investigate the deformation zone below imprints have been made over the whole range of indentation depths, from micro- down to nanoindentations, whereas EBSD examinations play an important role. To date, the performed EBSD investigations have stopped at an indentation depth of about 1 μm.[6,7] The present work extends the range of EBSD examinations down to indentation depths as small as 300 nm. For this purpose, EBSD investigations of the microstructure and texture below cube corner indentations in copper down to 300 nm indentation depth are presented. Furthermore, an explanation of the deformation mechanisms occurring during indentation as well as their consequences for the indentation size effect (ISE) is suggested and compared with experimental results.

A.2 Experimental details and materials

Single crystals of copper with a $\langle 1\bar{1}0 \rangle \{111\}$ orientation were prepared by wet grinding and mechanical polishing. To remove any deformation layer produced during mechanical polishing the $\{111\}$ surface planes used were subsequently electropolished. The plane perpendicular to the $\{111\}$ surface was carefully mechanically polished in order to obtain a sharp edge. Several indentations were produced in the

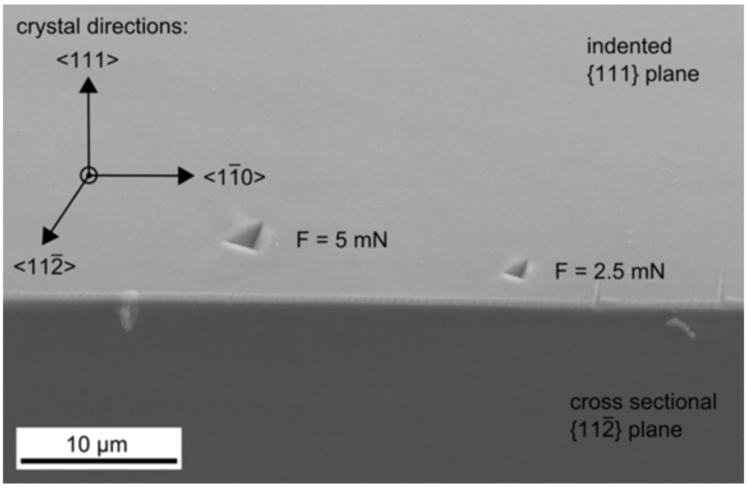

Figure A.1: SEM micrograph showing indentations placed in the vicinity of a sample edge before depositing a protection layer and cross-sectioning. The inset in the top left part displays the corresponding crystal directions.

vicinity of the specimen edge with loadings between 500 μN and 10 mN (see Figure A.1). The experiments were performed with a Hysitron TriboScope fitted with a cube corner indenter exhibiting a tip radius of about 40 nm. Cross-sections through the center of the indentations were fabricated using a FIB workstation (LEO 1540 XB). To protect the imprint against damage caused by the impact of Ga^+ ions a approximately 500 nm thick layer of tungsten was deposited. Before depositing the protection layer the center of the indentation was marked in order to obtain the cross-section right through the middle of the imprints. A milling current of 10 nA was used to remove material in front of the indentation. In the last milling step the current was set to 500 pA for the large imprints and 200 pA for the smaller ones. Subsequently, EBSD investigations of the polished cross-sections were performed using a field emission SEM (LEO 1525) equipped with an EDAX EBSD system. Due to changes in the crystal orientation caused by plastic deformation, the plastically deformed zone can be visualized. The accuracy of the absolute orientation measurement is 2-3°, while the relative misorientation can be measured with a precision of 0.5°. The scans were performed with a step size of 20 nm, resulting in ASCII files containing 8000-100,000 orientation data points. The orientation deviation was calculated using EBSD analysis software. To ensure proper pattern indexing, polishing of the cross-sections and EBSD mapping was performed within a period of 24 h.

The Hysitron TriboScope was also used to determine the indentation modulus and the hardness of the material at loads between 40 μN and 10 mN. To get accurate results a calibrated area function of the cube corner indenter as well as a correct value of the machine compliance is required. For these purposes, the procedure outlined by Oliver and Pharr[25] was applied. For all indentations a load-time sequence consisting of 5 s of loading to maximum load, holding at peak load for 20 s in order to minimize creep effects, and an unloading part of 17 s, including a holding period of 10 s at 10% of the maximum load was used. Three to five separate indentations were made for every selected indenter load. The presented results are an average of these indentations. The error bars in Figures A.8, A.9 and A.12 represent the standard deviation of each set of measurements.

Additionally, a TEM foil was prepared using the FIB workstation. Again, the center of the imprint was marked and a protection layer was deposited. By cutting two trenches on each side of the imprint, a lamella with a thickness of about 2 μm including the indentation was fabricated. After lifting out, the lamella was thinned to electron transparency using Ga$^+$ ions with a maximum acceleration voltage of 30 or 5 kV. TEM observations were made on a Philips CM12 TEM operating at 120 kV.

A.3 Results

Figure A.2 shows an SEM image of a readily polished cross-section through an imprint indented with a maximum load of 2.5 mN. On these cross-sections EBSD mapping was performed and the acquired data were used to calculate the misorientation angles relative to the undeformed single crystal. To visualize the orientation changes and consequently the dimensions of the deformation-induced zone, the calculated angles were plotted in misorientation maps, where crystal orientation changes can be identified using a color code.

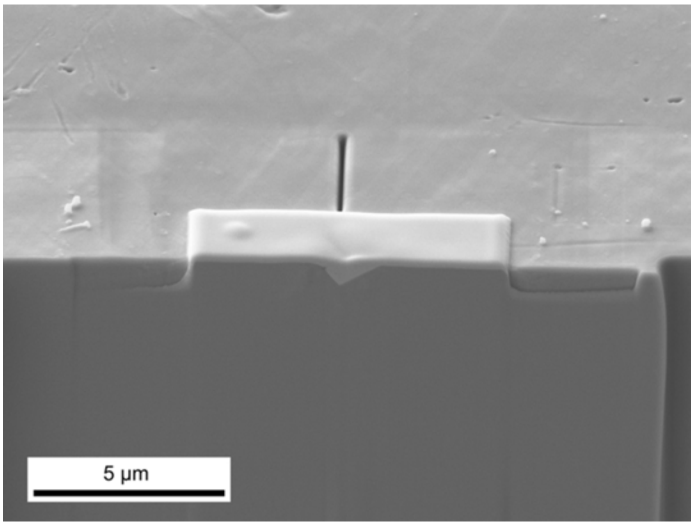

Figure A.2: SEM micrograph showing an inclined view of a readily polished cross-section through the middle of a 2.5 mN indentation. The image was taken using secondary electrons.

Figure A.3 shows misorientation maps of sectioned imprints indented at five different loads. A sketch showing how the indentations were cut is included at the

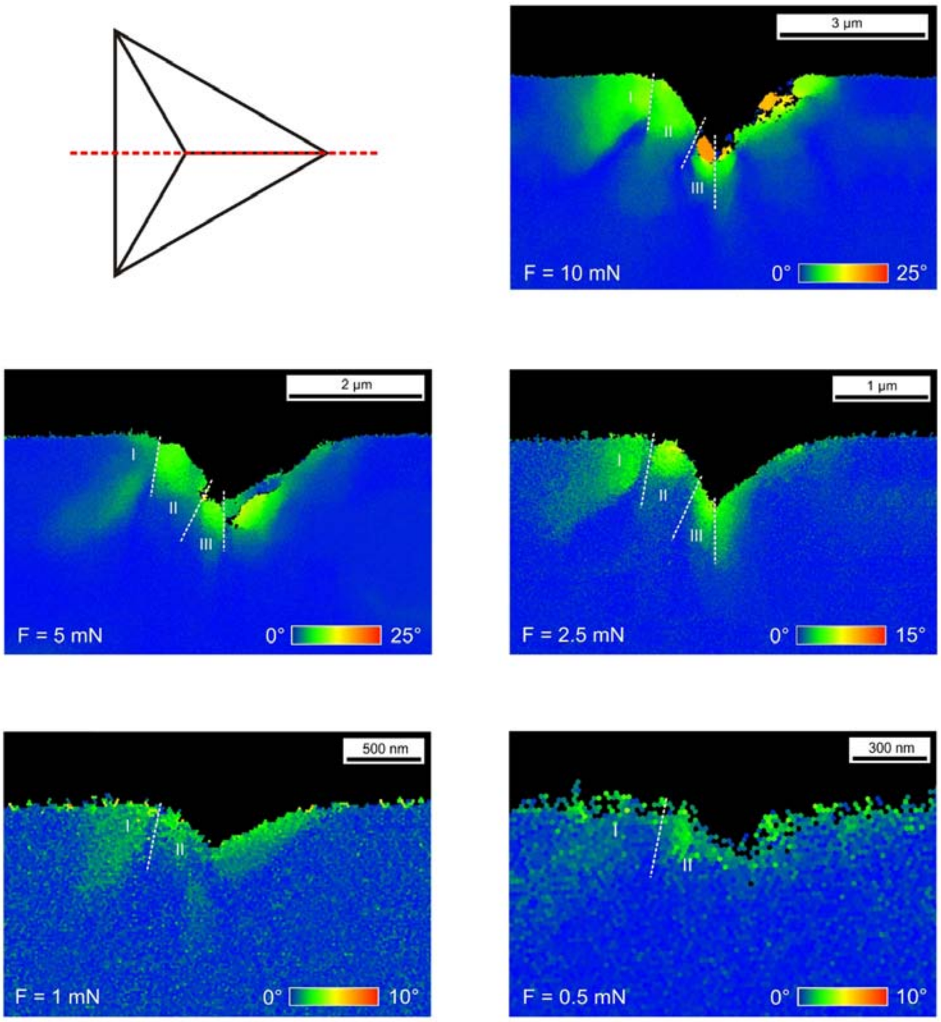

Figure A.3: Misorientation maps of indentations in copper for loads of 10, 5, 2.5, 1 and 0.5 mN. The sketch in the upper left part shows where the cross-sections through the indentations were placed. The Roman numerals in the misorientation maps denote characteristic regions.

upper left corner. On the left-hand side the imprint is cut through the face of the indentation, while on the right-hand side the cross-section proceeds through the edge of the cube corner imprint. Since it can not be ensured that the cross-section runs exactly through the indentation edge only the region below the indentation face as well as the area beneath the indenter tip is considered. Consequently, mirroring the left-hand side of the deformation pattern along the indentation symmetry axis would result in a rotation pattern comparable to that of a wedge indentation. To characterize the deformation zone below the indentation and to make discussion easier, the deformed area is coarsely divided into different sections. For indentations made with loads greater than 2.5 mN the deformation zone is divided into three characteristic regions, whereas the deformed area found below imprints made with lower loads consists of only two parts. In the following the deformation zone of the largest imprint as well as that of the smallest is analysed in detail.

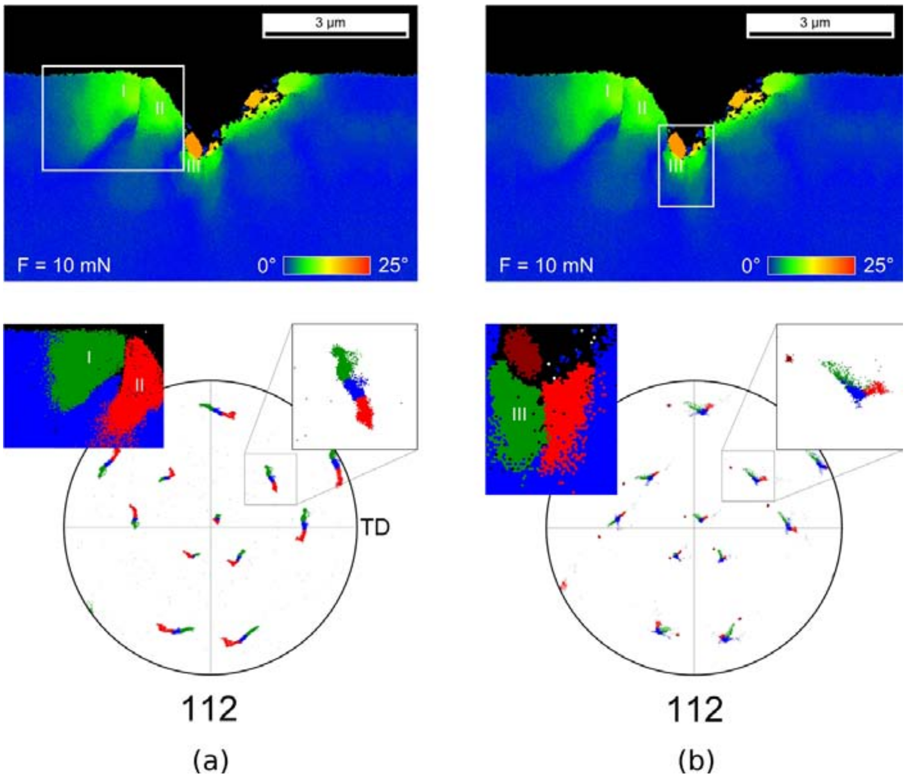

(a) (b)

Figure A.4: Misorientation maps and 112 pole figures of a 10 mN imprint. The insets show the deformation pattern and the rotational direction of the regions containing the indenter flank (a) and the indenter tip (b).

Figure A.4 presents the misorientation maps and corresponding pole figures of an indentation made with a load of 10 mN. Since the indentation direction was $\langle 111\rangle$ and the sample edge $\langle 1\bar{1}0\rangle$, the examined plane belong to the $\{11\bar{2}\}$ system. As can be seen, section I, located on the left-hand side directly under the sample surface, shows a rotation pattern with a huge lateral expansion (Figure A.4 (a)). Taking all points of section I (dark green points in the inset of Figure A.4 (a)) and plotting them in a 112 pole figure shows a counter-clockwise rotation around a $\langle 11\bar{2}\rangle$ axis. Adjacent to section I and directly beneath the indenter flank is another deformation-induced rotation pattern. This region, denoted section II, is rotated contrary to section I. Analyzing the pole figure of section II (red points in the inset of Figure A.4 (a)) reveals a clockwise rotation of the region around the $\langle 11\bar{2}\rangle$ axis. Both deformation patterns are separated by an arrangement of geometrically necessary dislocations (GNDs) inclined about 10° to the indentation direction and running from the intersection sample surface-indentation face down into the crystal.

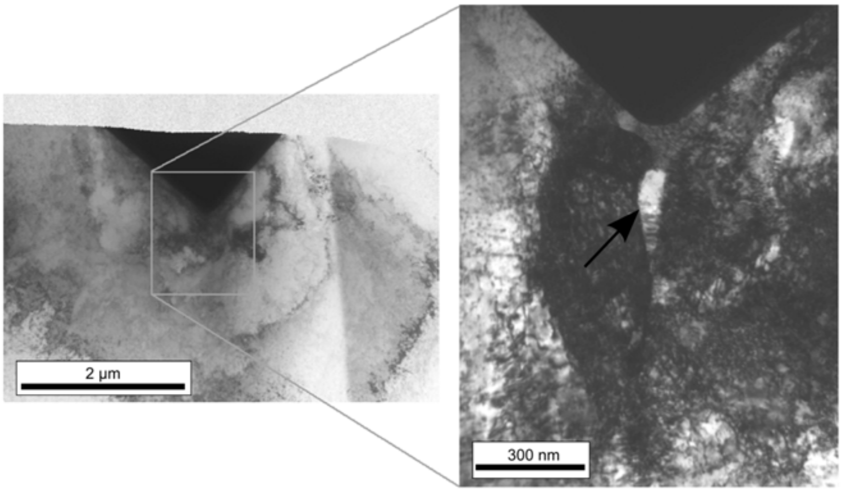

Figure A.5: TEM micrograph of a 10 mN indentation. The left part shows the whole imprint while in the right part the indentation tip is enlarged. The arrow marks a formed subgrain directly below the indenter tip.

The area below the indenter tip, denoted section III, which contains another deformation pattern, is presented in Figure A.4 (b). As can be seen in the pole figure, section III is twisted in direct opposition to section II and in the same direction as the deformation pattern found in section I. A single domain with a very high misorientation of about 22°, which can be observed in the misorientation map, is also plotted in the pole figure (brown points in Figure A.4 (b)). It would appear that subgrain formation induced by the regionally high dislocation density beneath the indenter tip occurs. To obtain more precise information about this area, TEM studies were performed. For this purpose, a cross-section through a 10 mN indentation was prepared and analysed. The TEM micrographs are shown in Figure A.5, in the left part of which an overall view of the imprint is presented. The right micrograph displays an enlarged view of the area around the indenter tip. Noticeable is a droplet-shaped zone (marked with an arrow in the right part of Figure A.5) enclosed by an area of high dislocation density. This fact verifies the possibility of subgrain formation directly under the indenter tip.

Studying the imprints with loads below 1 mN yielded slightly different results (see Figure A.6). In the same way as observed for high load imprints, two sections (denoted by I and II) separated by an arrangement of geometrically necessary dislocations can be found. Information about the orientation changes are shown in the added 112 pole figure. As can be seen, section I is rotated counterclockwise around a $\langle 11\overline{2} \rangle$ rotation axis, whereas section II is twisted clockwise. No region below the indenter tip containing an opposite twisted deformation pattern, comparable to those found at the high load imprint in section III, could be observed. The deformation-induced pattern of section II rather extends to the indenter tip.

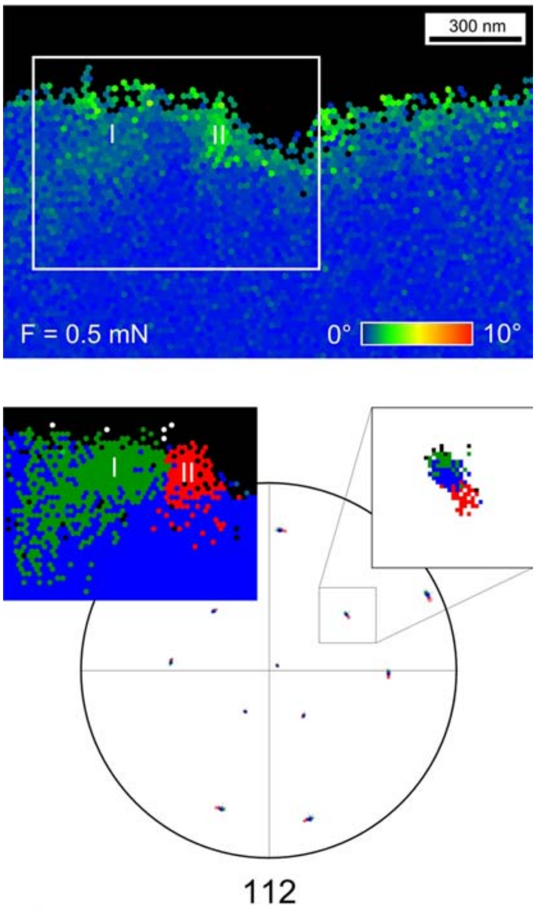

Figure A.6: Misorientation map and 112 pole figure of a 0.5 mN imprint. The insets show the deformation pattern and rotational direction of a region containing the indenter flank and the indenter tip.

In order to obtain information about the orientation distribution across the indentation flank, the misorientation along lines tilted 50° to the sample surface was measured. This angle was chosen to get a misorientation profile only through section II, not across the boundary between sections I and II. The resulting misorientation profiles are presented in Figure A.7. As can be seen, for the 10 and 5 mN imprints a misorientation plateau close to the indenter flank appears. The found plateau value is approximately 8° for the 10 mN indentation and about 5° for the 5 mN imprint. Following the orientation deviation plateau, the misorientation decreases exponentially towards the undeformed crystal. For smaller imprints, i.e. 2.5, 1 and 0.5 mN, no misorientation plateau could be found. However, starting directly at the indenter flank, the misorientation decreases exponentially.

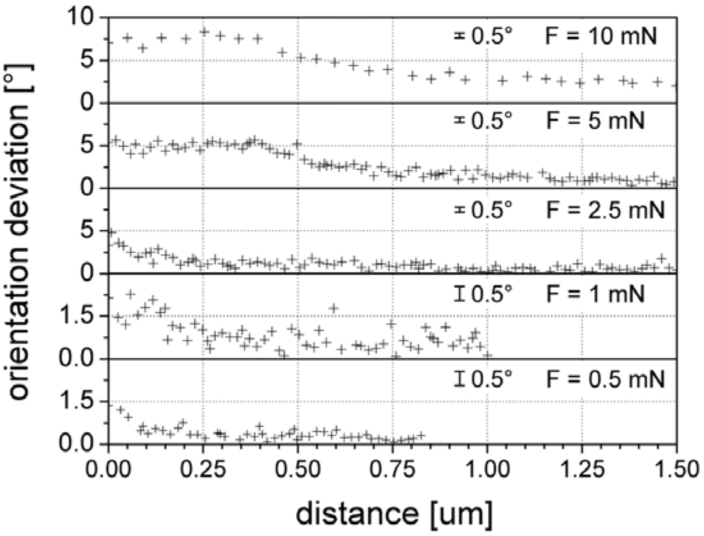

Figure A.7: Misorientation profiles across the indenter flank for indentations performed with loads of 10, 5, 2.5, 1 and 0.5 mN. The error for each individual datum point is 0.5°, as indicated in the diagram.

Figure A.8 presents the results of the hardness measurement obtained for the {111} surface of the copper single crystal. As can be seen, the dependence of the hardness on contact depth is highly pronounced. Starting with a value of 2.75 GPa at an indentation depth of 35 nm, the hardness decreases as the load increases, reaching a plateau of approximately 1.1 GPa. The reduced indentation modulus of the material can be found to be approx. 125 GPa and is rather constant over the whole measuring range. It is common to use the modulus as an indicator to check if the value of the compliance is correct. An incorrect compliance would result in a non-constant indentation modulus and erroneous hardness values. Since only at small indentation depths increased scatter of the modulus data appear, the compliance used seems to be correct. Analyzing the error which causes the scatter of the modulus data shows that inaccuracies in depth measurement influence the indentation modulus to a lesser extent than the hardness. Since the scatter of the

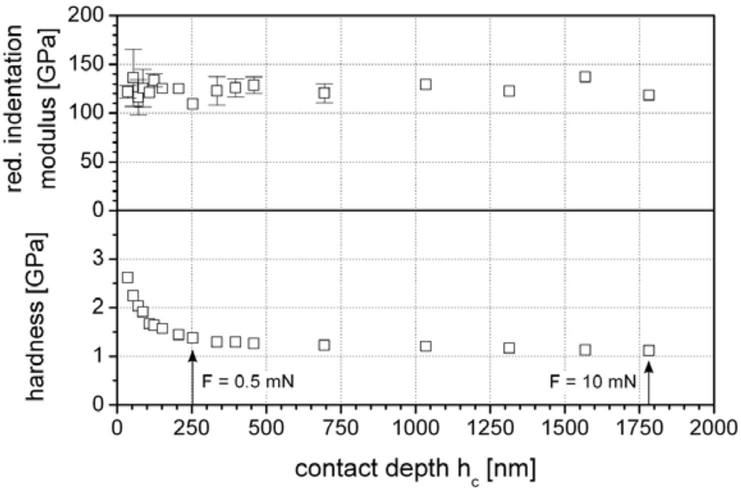

Figure A.8: Hardness and reduced indentation modulus as a function of the contact depth. The arrows mark the hardness value for the smallest and largest imprints investigated in the course of this work. Error bars are inserted only for those datum points where the error bar is larger than the size of the symbol.

modulus values is not reflected in the hardness data, improper depth measurement is not responsible for the observed modulus scatter. Instead, the spreading modulus data can be linked to thermal drift effects, which occur preferentially at low indentation depths where the ratio between thermal induced indenter displacement and total displacement is large. The fact that the modulus is dependent on not only the indentation depth can be seen in the following equation:

$$E_r = \frac{S\sqrt{\pi}}{2\sqrt{A_c}} \tag{A.1}$$

where A_c is the contact area and S is the contact stiffness which corresponds to the slope of the elastic unloading dP/dh. For highly plastic materials, such as copper, a very steep slope of the elastic unloading dP/dh is found. Due to the steepness of the curve, small variations in the slope cause large changes in the contact stiffness and consequently in the reduced indentation modulus. Especially at low indentation depths, such slope changes caused by thermal drift effects occur. The result is the observed scatter of the modulus data shown in Figure A.8.

Figure A.9 (a) displays a graph where the square of the hardness is plotted against the reciprocal indentation depth. An enlarged view of the graph focusing on indentation depths greater than 167 nm is shown in Figure A.9 (b). Based on an approximation of Nix and Gao[26] that all GNDs are stored in a hemispherical volume below the indenter tip, the relation between H^2 and $1/h_c$ should be linear over the whole

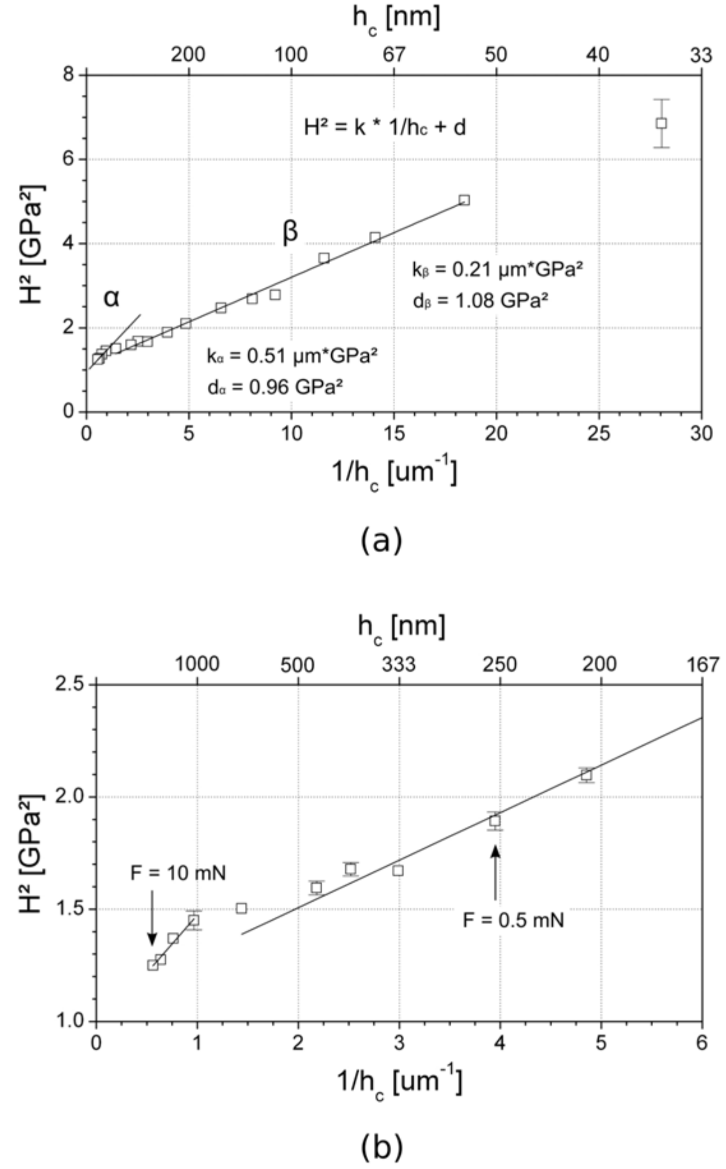

Figure A.9: Application of the Nix-Gao model to the measured hardness values: H^2 vs. $1/h_c$ plot (a) for the whole measurement range and (b) for depths larger than 167 nm. Error bars are inserted only for those datum points where the error bar is larger than the size of the symbol.

depth range. In contrast, a bilinear characteristic with different slopes for indentation depths greater (regime α in Figure A.9 (a)) and smaller than 1 μm (regime β in Figure A.9 (a)) was found. Analyzing the slopes delivers 0.51 μm GPa^2 for regime α and 0.21 μm GPa^2 for regime β. The square root of the axis intercept corresponding to the macroscopic hardness H_0 is approximately 1 GPa for both regimes. It should be noted that the datum point of the smallest imprint was excluded from the analysis since the associated error was disproportionately high.

A.4 Discussion

Studying misorientation maps of various sized indentations shows that accommodating the displacement imposed by an indenter is accomplished by changes in the crystal orientation. However, the way the accommodation is achieved changes with reducing indentation depth. For large imprints huge orientation changes can be found, while for shallow indentations the appearing misorientation is only minor. Consequently, the question is raised how the observed orientation changes can be realized. A possible arrangement of geometrically necessary dislocations explaining the observed behavior for large indentations is schematically shown in Figure A.10. The suggested arrangement should accommodate the shape of the indentation as well as explain the observed crystal orientation changes. Large indentations are always accompanied by the occurrence of a huge and far-reaching shear stress field. Consequently pre-existing sources located near the indenter flank in the region denominated A in Figure A.10 can be activated and are able to emit dislocation loops. For the sake of simplicity, it is assumed that only two types of slip planes can generate dislocations, where one is perpendicular to the indenter flank and the other parallel to it. The slip planes are chosen in such a way that the emitted dislocations can build up the observed crystal orientation change, i.e. the schematically indicated dislocations are geometrically necessary in terms of changes of orientation. In reality, the slip planes might differ significantly from those suggested in Figure A.10; however, the stored dislocations in the different regions have to cause the same effect as the indicated dislocations. Thus dislocation loops which are generated on slip planes perpendicular to the indenter flank start to move towards the indenter and pile-up in front of it, producing the required large orientation changes (Figure A.10, region 2). The formation of the pile-up, on the other hand, induces a significant back stress to the sources and thus impedes further dislocation generation. Dislocations exhibiting a contrary sign move in the opposite direction into a region denominated 4 and, since they are very widely spread, the induced orientation gradient is only slight. Dislocation loops generated on the second type of introduced slip plane, parallel to the indenter flank, move into the region below the indenter tip. Due to a change in the shear stress field, they are not able to overcome the center region. Instead they form a pile-up at the “symmetry” line, causing the observed misorientation at the indenter tip (Figure A.10, region 3). The other parts of the loops move towards the free surface, where few of them exit the material. But the majority of the dislocations arrange themselves in the region where the shear stress goes to zero by forming a "small angle grain boundary"-like structure, which is responsible for the misorientation changes in region 1. Although the model presented is only a simplified arrangement of dislocations, it is in good agreement with the crystal rotation directions of the different regions found in the EBSD analysis (see Figure A.4).

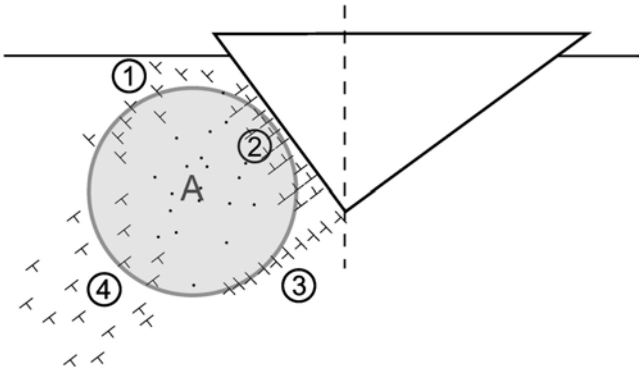

Figure A.10: Dislocation model describing the indentation process of large imprints. The letter A denotes a region where pre-existing sources (dots in region A) can be activated and emit dislocations. The numbers 1-4 denominate regions containing dislocations with characteristic sign.

Considering shallow indentations, on the other hand, poses the question why the described mechanisms become less important with decreasing indentation depth. As can be seen, lowering the indentation depth is directly linked to a diminishment of region A in Figure A.10 and consequently to a decrease in the number of activatable dislocation sources. The result is an increase in the back stress originating from the dislocations piled up in regions 2 and 3, which consequently impedes the generation of further dislocation loops. Since the emission of dislocations is hindered, other mechanisms, like the generation of dislocations lateral to the indentation, become more important. These mechanisms are heterogeneous dislocation generation induced by surface defects like fractured oxide layers as well as spontaneous dislocation nucleation, which is well known from molecular dynamic simulations and appears especially at very low indentation depths.[27–30] A schematic arrangement of the geometrically necessary dislocations accommodating a shallow imprint is suggested in Figure A.11. The emitted dislocations form a kind of prismatic loop which moves on the slip planes that are arranged very close to each other. As a consequence, the recently generated dislocations push the previously created ones towards the bulk material. However, for extremely shallow indentations the segment length of the dislocations generated in region B becomes very small and as a consequence the stress required to push the dislocations away from the indenter flank is pretty high. Increasing the indentation depth and consequently the segment length of the dislocations causes the observed decrease in hardness. It can be seen that such an arrangement induces only slight orientation changes, which is in good agreement with

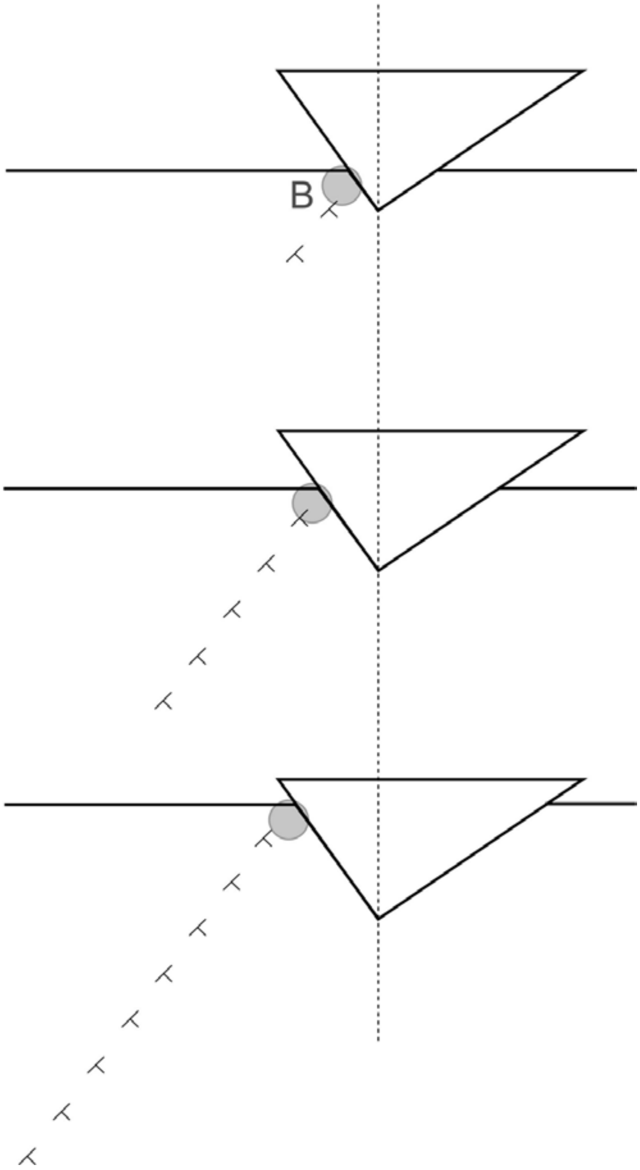

Figure A.11: Dislocation model showing a sequence of events occurring during indentation of shallow imprints. The letter B denotes a region where dislocation generation preferably take place.

the experimental observations (see Figures A.6 and A.7). The suggested model is also supported by results found by Minor et al.,[24] where dislocation loops nucleated in a defect-free volume are not contained in a predefined plastic zone. Instead, they propagate far into the bulk, producing a plastic zone differing from those proposed by classical continuum mechanics models. Atomistic simulation studies of the initial stages of nanoindentation show similar results. As the simulations demonstrate, dislocation loops are nucleated in regions directly beneath the surface and propagate towards the undeformed crystal as the load increases.[31–34]

The bilinear behavior of the hardness data (Figure A.9) as well as the misorientation maps (Figure A.3) indicate a change in the deformation mechanism. For large indentations it seems that the pile-up model described in Figure A.10 is responsible for the indentation size effect. Examining the suggested model (Figure A.10) reveals similarities to the Hall-Petch effect. However, there are also some differences: in a polycrystalline material the pile-ups that occur at a boundary have to trigger plasticity in the neighboring grains, whereas the pile-ups in this case have to accommodate the shape of the indenter. Contrary to polycrystalline materials, the deformation zone below an indentation (region A in Figure A.10) is highly bounded on only one side, namely to the indenter flank. The other sides are less bounded, due to either a change in the shear stress field, which forms only a weak barrier (regions 1 and 3), or the necessity of pushing previously generated dislocations into the bulk material (region 4). Due to the similarities between both models, the hardness should follow the Hall-Petch relation[35,36]

$$\sigma_y = \sigma_0 + k_{HP}\frac{1}{\sqrt{D}} \tag{A.2}$$

where the grain size is substituted by D, the diameter of region A (see Figure A.10). Both, k_{HP} the Hall-Petch parameter and σ_0 the intrinsic yield strength in the absence of grain size effects are constants that depend on the nature and state of the crystal. Using Tabors rule[37] to convert the hardness into the corresponding flow stress σ_y and assuming that the size of region A is proportional to the indentation depth h, the Hall-Petch relation can be easily rewritten as

$$(H - 3\sigma_0)^2 = k_1\frac{1}{h} \tag{A.3}$$

where k_1 is a constant. As can be seen, Eq. A.4 seems to be similar to the Nix-Gao relation

$$H^2 - H_0^2 = k\frac{1}{h} \tag{A.4}$$

where k is the slope of the hardness in the Nix-Gao plot and H_0 is the macroscopic hardness. It should be noted that the hardness can follow both relations only if σ_0

and H_0 are 0. However, it is evident from Figure A.9 that $H_0 \neq 0$; nevertheless, we have plotted the hardness data in terms of the Hall-Petch relation.

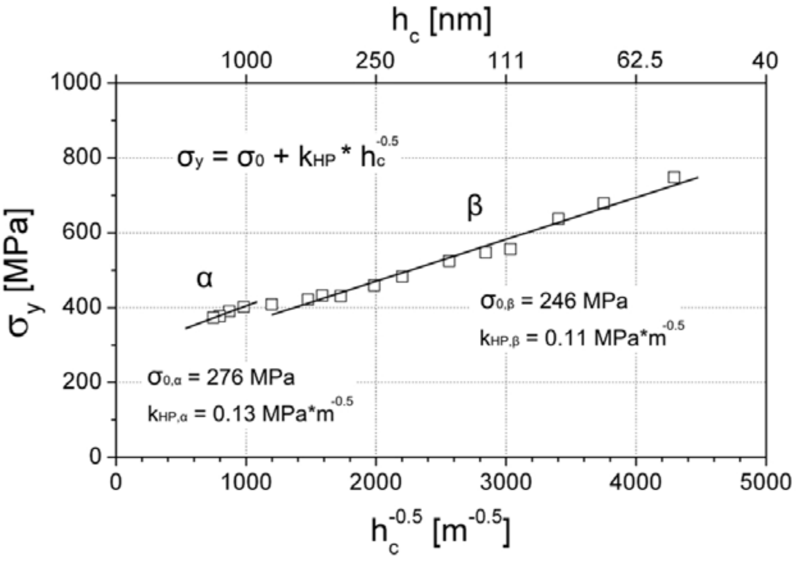

Figure A.12: Hall-Petch plot of the effect of contact depth h_c on the flow stress of Cu. The flow stress was calculated using Tabors rule, where $\sigma_y = H/3$. Since the error bars are smaller than the datum points they are not inserted in the graph.

The resulting σ_y vs. $h_c^{-1/2}$ plot, including the corresponding linear fits of the data, is presented in Figure A.12. As can be seen, the regimes identified in the Nix-Gao plot show a linear trend in the Hall-Petch plot too. The linear behavior of the flow stress in regime α supports the existence of a pile-up-based dislocation model for the accommodation of large imprints. However, the linear trend of the flow stress in regime β was not expected. It seems that the mechanism which describes the indentation process of shallow imprints is also based on dislocation pile-ups. Thus, both regimes are associated with mechanisms that are based on the pile-up of dislocations. This is in good agreement with the models suggested in the course of this work (see Figures A.10 and A.11). Examination of the linear fits shows that the Hall-Petch parameter of regime α ($k_{HP,\alpha}$) is 0.13 MPa m$^{-1/2}$, similar to the reported value of 0.12 MPa m$^{-1/2}$.[38] The Hall-Petch parameter of regime β ($k_{HP,\beta}$) however, is 0.11 MPa m$^{-1/2}$, which is lower than the parameter of regime α. The lower value of $k_{HP,\beta}$ may be explained by a diminished number of barriers which pile-up the emitted dislocations (see Figure A.11). In addition to the differing slopes, the σ_0 values are also different for both regimes. For large indentations (regime α) $\sigma_0 = 276$ MPa, while for shallow imprints (regime β) the intrinsic yield strength is 246 MPa.

The differences might be induced by the strain sensitivity of σ_0. As Armstrong et al.[39] demonstrated, σ_0 increases with increasing strain.

The results presented show the importance of the dislocation arrangements and how they change with varying length. However, additional experimental analysis and modeling work will be necessary to understand the indentation process over all depth ranges.

A.5 Summary and conclusions

Several cross-sections through nanoindentations in copper single crystals were prepared using a FIB workstation. The EBSD technique was applied to examine the fabricated cross-sections and to get information about the deformed volume beneath the indentations. Studying the misorientation maps thus obtained revealed for large indentations a highly confined rotation pattern consisting of three characteristic sections, while for shallow indentations only two, more spacious, patterns were found. It is assumed that the apparent change in the structure of the deformation zone is linked to a variation in the deformation mechanism. Indications for a mechanism change were found not only in the results of the EBSD investigations; the analysis of the measured hardness data using Nix-Gao plots yielded the same conclusions. The Nix-Gao plot shows a bilinear relationship between the square of the hardness and the reciprocal indentation depth, with hardness values for large imprints lying on the steep part of the curve and those for shallow indentations lying on the gently inclining part. To explain the observed changes, two models based on possible dislocation arrangements are presented. The model for large imprints and that for the shallow indentations show very good agreement with the experimental findings.

Bibliography to paper A

[1] Mulhearn TO. J Mech Phys 1959;7:85.

[2] Hill R, Lee EH, Tupper SJ. Proc R Soc London Ser A 1947;188:273.

[3] Keh AS. J Appl Phys 1960;31:1538.

[4] Tsui TY, Vlassak J, Nix WD. J Mater Res 1999;14:411.

[5] Inkson BJ, Steer T, Möbus G, Wabner T. J Microsc 2000;201:256.

[6] Zaafarani N, Raabe D, Singh RN, Roters F, Zaefferer S. Acta Mater 2006;54:1863.

[7] Kiener D, Pippan R, Motz C, Kreuzer H. Acta Mater 2006;54:2801.

[8] Zielinski W, Huang H, Gerberich WW. J Mater Res 1993;8:1300.

[9] Zielinski W, Huang H, Venkataraman S, Gerberich WW. Philos Mag A 1995;72:1221.

[10] Le Bourhis E, Patriarche G. Philos Mag Lett 1999;79:805.

[11] Chiu YL, Ngan AHW. Acta Mater 2002;50:2677.

[12] Patriarche G, Le Bourhis E, Faurie D, Renault PO. Thin Solid Films 2004;460:150.

[13] Wo PC, Ngan AHW, Chiu YL. Scipta Mater 2006;55:557.

[14] Wo PC, Ngan AHW, Chiu YL. Scipta Mater 2007;56:323.

[15] Saka H, Abe S. J Electron Microsc 1997;1:45.

[16] Ando M, Katoh Y, Tanigawa H, Kohyama A. J Nucl Mater 1999;271272:111.

[17] Lloyd SJ, Molina-Aldareguia JM, Clegg WJ. Philos Mag A 2002;82:1963.

[18] Mogilevsky P. Philos Mag 2005;85:3511.

[19] Lloyd SJ, Castellero A, Giuliani F, Long Y, McLaughlin KK, Molina-Aldareguia JM, et al. Proc R Soc London Ser A 2005;461:2521.

[20] Viswanathan GB, Lee E, Maher DM, Banerjee S, Fraser HL. Acta Mater 2005;53:5101.

[21] Long Y, Giuliani F, Lloyd SJ, Molina-Aldareguia J, Barber ZH, Clegg WJ. Composites Part B 2006;37:542.

[22] McLaughlin KK, Stelmashenko NA, Lloyd SJ, Vandeperre LJ, Clegg WJ. Mater Res Soc Symp Proc 2005;841:R1.3.

[23] Minor AM, Lilleodden ET, Stach EA, Morris Jr JW. J Electron Mater 2002;31:958.

[24] Minor AM, Lilleodden ET, Stach EA, Morris Jr JW. J Mater Res 2004;19:176.

[25] Oliver WC, Pharr GM. J Mater Res 1992;7:1564.

[26] Nix WD, Gao H. J Mech Phys Solids 1998;46:411.

[27] Li J, Van Vliet KJ, Zhu T, Yip S, Suresh S. Nature 2002;418:307.

[28] Gouldstone A, Van Vliet KJ, Suresh S. Nature 2001;411:656.

[29] Van Vliet KJ, Li J, Zhu T, Yip S, Suresh S. Phys Rev B: Condens Matter 2003;67:104105.

[30] Zhu T, Li J, Van Vliet KJ, Ogata S, Yip S, Suresh S. J Mech Phys Solids 2004;52:691.

[31] Lilleodden ET, Zimmerman JA, Foiles SM, Nix WD. J Mech Phys Solids 2003;51:901.

[32] Zimmerman JA, Kelchner CL, Klein PA, Hamilton JC, Foiles SM. Phys Rev Lett 2001;87:165507.

[33] Kelchner CL, Plimpton SJ, Hamilton JC. Phys Rev B 1998;58:11085.

[34] Kreuzer HGM, Pippan R. Acta Mater 2007;55:3229.

[35] Hall EO. Proc Phys Soc B 1951;64:747.

[36] Petch NJ. J Iron Steel Inst 1953;174:25.

[37] Tabor D. Proc R Soc A 1947;192:247.

[38] Hall EO. Yield point phenomena in metals and alloys. London: Macmillan; 1970.

[39] Armstrong R, Codd I, Douthwaite RM, Petch NJ. Philos Mag 1962;7:45.

B

The deformation-induced zone below large and shallow nanoindentations – A comparative study using EBSD and TEM

M. Rester, C. Motz and R. Pippan

Erich Schmid Institute of Materials Science, Austrian Academy of Sciences,
A–8700 Leoben, Austria

Abstract

The paper addresses the comparison of the deformation-induced zone beneath nanoindentations obtained by electron backscatter diffraction (EBSD) and transmission electron microscopy (TEM). Since EBSD is associated with resolutional restrictions, especially at very small scan sizes, it is not known how accurate the deformed volume beneath the imprints can be characterized. For these purposes, cross-sectional EBSD and TEM samples of nanoindentations were fabricated by means of a focused ion beam (FIB) workstation, analyzed, and subsequently compared among each other. For large indentations as well as for shallow ones, a very good agreement of the determined zones was found. The results of the EBSD and TEM experiments were also used to characterize the deformation-induced volume. In the EBSD maps of the large indentations, strongly confined deformation patterns were found while for the shallow indentations the observed patterns are ambiguous. The TEM micrographs and additionally performed selected area electron diffraction (SAED) support these facts and give insight into the dislocation structure of the deformation zone.

B.1 Introduction

It is now well-known that hardness of metallic materials in the sub-micron regime is a strong function of the indent size, i.e. with decreasing indentation depth the indentation hardness increases.[1–3] This phenomenon is referred to as the indentation size effect (ISE). Nix and Gao have used the concept of geometrically necessary dislocations (GNDs) and the Taylor dislocation model in order to explain the observed behavior.[4] One assumption made in the Nix-Gao (N-G) model is, that GNDs are confined within a hemispherical volume which scales with the contact radius. Recent transmission electron microscopy (TEM) studies have shown that this assumption is questionable. Rather, the plastically deformed zone expands in a non-self similar manner far beyond the suggested hemispherical volume.[5,6] Similar results were found in studies, which investigated the deformation zone below nanoindents in copper by means of electron backscatter diffraction (EBSD).[7,8]

However, using EBSD technique is always accompanied by a limited spatial resolution and the restriction that only relative crystal orientation changes larger than 0.5° can be measured.[9] Due to these limitations it is unclear how accurate the deformation zone beneath imprints can be determined by means of the EBSD technique. In order to respond to this question the plastically deformed zones obtained by TEM and EBSD technique are compared. Furthermore, the formed dislocation structure below the imprints is investigated, with a special focus on how the dislocation arrangement changes when the indentation load is increased. The acquired findings were subsequently used, to discuss how deformation mechanisms in such limited volumes may proceed.

B.2 Experimental procedure

Copper $\langle 1\bar{1}0\rangle\,\{111\}$ single crystals were prepared by wet grinding and mechanical polishing. Subsequently, to remove any deformation layer produced during previous polishing steps the surface plane was electropolished. To obtain a sharp edge, the plane perpendicular to the $\{111\}$ surface was carefully mechanically polished. A Hysitron TriboScope fitted with a cube corner indenter was used to produce indentations with loadings between 0.5 mN and 10 mN near the polished edge. The tip radius of the used indenter was approximately 40 nm. Using a focused ion beam workstation (LEO 1540 XB), cross-sections through the center of these imprints were fabricated. To protect the imprints against ion damage a tungsten layer with a thickness of about 500 nm was deposited. Prior to the deposition of the protection layer, the centers of the imprints were marked in order to obtain cross-sections which proceed right through the middle of the indent. On the readily polished cross-sections EBSD investigations were performed using a LEO 1525 field emission scanning electron microscope (SEM) equipped with an EDAX EBSD system. Since plastic deformation causes crystal orientation changes, the plastically deformed zone surrounding an imprint can be visualized. The scans on the cross-sections were performed with a step size of 20 nm providing ASCII files of 8000–100,000 orientation data points. Absolute orientations can be measured with an accuracy of approximately 2–3°, while the error in determining relative orientation measurements is in the order of 0.5°.

Using the FIB workstation, in a next step cross-sectional TEM samples were prepared. Again, the nanoindenter was used to produce imprints with loads of 10 mN and 0.5 mN, respectively. The center of the imprint was marked and a protection layer deposited. Subsequently, two trenches on each side of the imprint were cut, resulting in a foil of about 2 μm thickness which contains the indentation. By means of a micromanipulator the foil was lifted out and fixed to a TEM sample holder. Using acceleration voltages of 30 kV and 5 kV, respectively, the foil was thinned to electron transparency. The reduced voltage of 5 kV was used to minimize ion damage in order to improve the quality of the TEM images. A Philips CM12 TEM operating at 120 kV was used for the analysis.

B.3 Results and discussion

The misorientation maps of sectioned indents for five different loads are shown in Figure B.1. Misorientations larger than 1° are colored in light gray in order to visualize the dimension of the deformation-induced zone. The scheme in the lower right corner shows, how the indentations were cut. As can be seen, on the left-hand side the imprint is cut through the indent face, while on the right-hand side the cross-section proceeds through the edge of the cube corner. Since it can not be ensured that the cross-section runs exactly through the indentation edge, only the region below the indentation face as well as the area beneath the indenter tip is investigated. Examination of the misorientation maps show for the 10, 5 and 2.5 mN a deformation-induced volume which consists of three characteristic sections, while for imprints made at lower loads only two of these sections can be found (roman numerals in Figure B.1). Noticeable is, that especially for the high load imprints the deformation-induced patterns are highly confined and section I and section II are separated by a sharp boundary. For the low load imprints, the deformed volume looks quite different. Apart from the fact that the deformed volume consists of only two characteristic sections, the deformation-induced patterns are no longer strongly confined. Rather, as the indentation load is decreased, they are getting more and more undefined. A further finding, which can be observed in all of the misorientation maps, is the high lateral extension oft the deformation-induced zone. Unlike as suggested by Nix and Gao, the deformed volume extends up to 2.5 times the imprints diameter.

However, considering the limited spatial resolution of the EBSD technique, it is not clear how accurate the deformation zone beneath the imprints is detected. In order to address this issue, the deformation-induced zone found in EBSD misorientation maps is compared to the deformation-induced structure detected in the TEM. For this purpose, cross-sectional TEM samples of a 10 mN and a 0.5 mN indent are

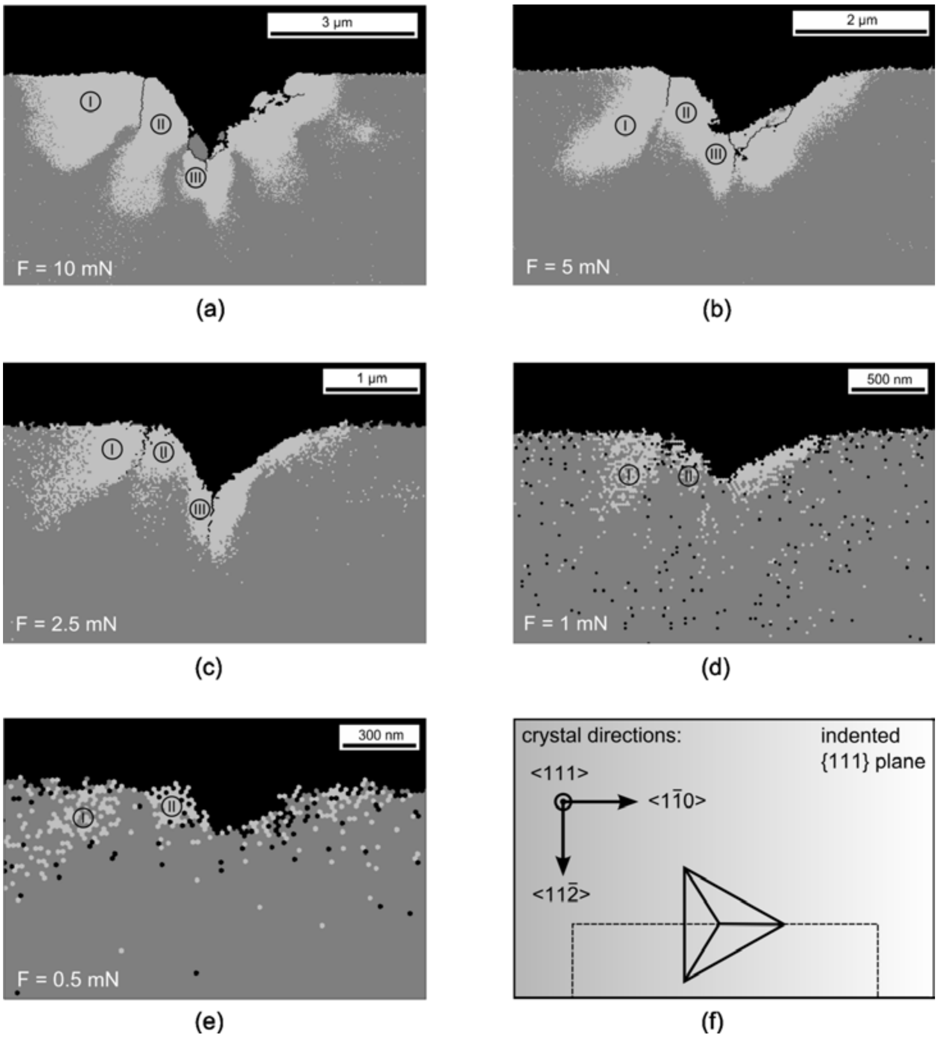

Figure B.1: (a)–(e) EBSD misorientation maps of indentations in copper for loads of 10, 5, 2.5, 1 and 0.5 mN. Misorientations greater than 1° are colored in light gray in order to visualize the dimensions of the plastically deformed zone. The roman numerals in the misorientation maps denote characteristic regions. (f) Scheme showing how the cube corner indentations were sectioned as well as the positions of the imprints with respect to the crystal orientation.

investigated. The resulting micrographs of the indentations taken with a $\bar{1}1\bar{1}$ two beam condition are shown in Figure B.2.

Examining the 10 mN imprint shows a characteristic dislocation pattern at the left-hand side of the cube corner indenter (Figure B.2 (a)). An enlarged view of this dislocation arrangement, which runs down towards the bulk crystal inclined about 10° to the sample surface, is presented in Figure B.2 (b). What can be seen is a very sharp boundary piling up dislocations on the right hand side, while the area on the left hand side is almost dislocation-free. The finding is consistent to the observations made in the EBSD misorientation map where a boundary, separating section I and section II, was as well detected. Another interesting area is the zone below the indenter tip which is shown enlarged in Figure B.2 (c). Notable in this region are dislocation-free zones surrounded by walls of high dislocation density. This verifies the existence of sub-grain formation in the area beneath the indenter tip. Looking to the right-hand side of the indent, a long drawn-out domain with only minor dislocation density is found (Figure B.2 (a)). It seems that here as well a kind of sub-grain formation occurred. However, only slight hints to the formation of sub-grains can be found in the EBSD misorientation maps. For the 10 mN indent in Figure B.1, a single domain of increased misorientation looking like a sub-grain, appears on the left-hand side of the indenter tip.

Examining the TEM micrographs of the 0.5 mN imprint (Figure B.2 (d)) shows a somewhat different picture. The sharp boundary of GNDs, found for the 10 mN imprint is for the 0.5 mN indent reduced to only a few dislocations (white ellipse in Figure B.2 (d)). Dislocation-free domains below the indenter tip, enclosed by walls of high dislocation density, can not be observed. Instead single dislocation loops surround the tip of the indentation. The small black dots, spread over the whole TEM sample are artifacts caused by Ga^+ ion damage during sample preparation. Reducing the acceleration voltage to 5 keV indeed diminishes the damage, the preparation of artifact-free samples, however, was not possible. Comparing the EBSD misorientation maps of the shallow imprint to the results found in the TEM micrograph, show surprisingly good agreement. Contrary to what was expected by the limited spatial resolution of the EBSD system, the characteristic features of the deformation zone were reproduced very well. Noticeable in Figure B.1 (e) is, that the boundary on the left hand side of the imprint is mapped not as a sharp line but as an ambiguous area. As might be expected this is not an effect of the limited spatial resolution of the EBSD system, but caused by the fact that section I and section II are separated by only few dislocations which induces only slight misorientation changes. The undefined shape of the deformation patterns can be attributed to the only low orientation gradients, too (Figure B.1 (e)).

However, to accommodate the shape of an indent many GNDs are necessary. Consequently, high misorientation gradients, especially for shallow imprints, would be expected. The findings obtained from EBSD and TEM show somewhat different results. Since only slight misorientation gradients were observed, the required GNDs seem to propagate far into the bulk material. To check this assumption, selected area electron diffraction (SAED) of interesting regions was accomplished using TEM.

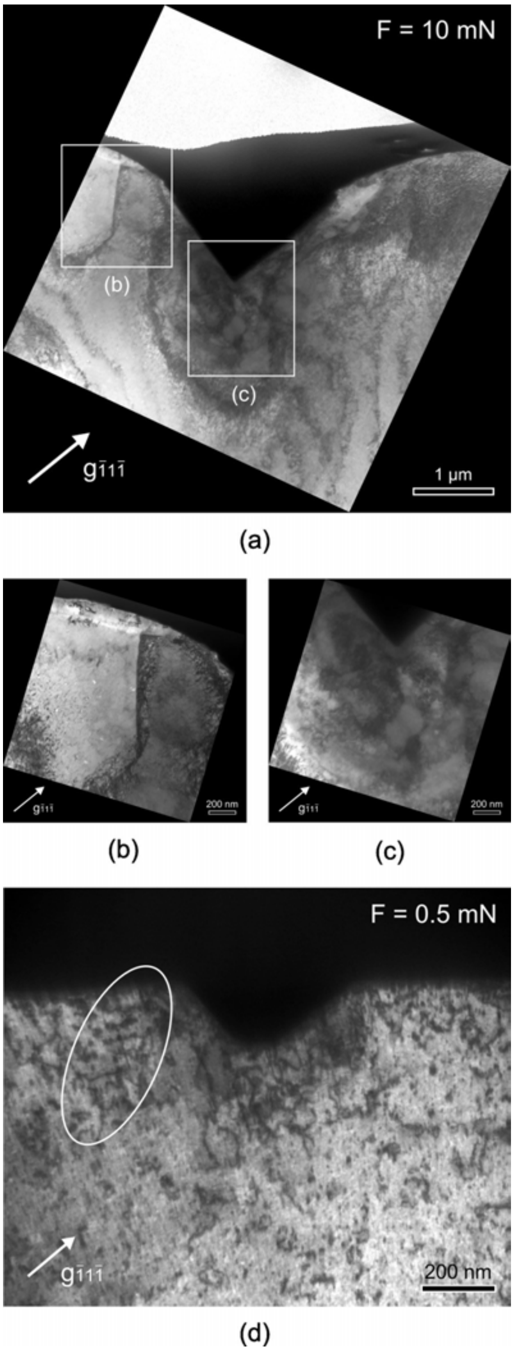

Figure B.2: (a) Cross-sectional TEM micrograph of a 10 mN indentation in a copper {111} single crystal taken with a $\bar{1}1\bar{1}$ two beam condition. The white rectangles mark regions of interest which are presented enlarged in (b) and (c). (d) Cross-sectional TEM micrograph of a 0.5 mN indentation in a copper {111} single crystal taken with a $\bar{1}1\bar{1}$ two beam condition. The white ellipse mark dislocations of special interest.

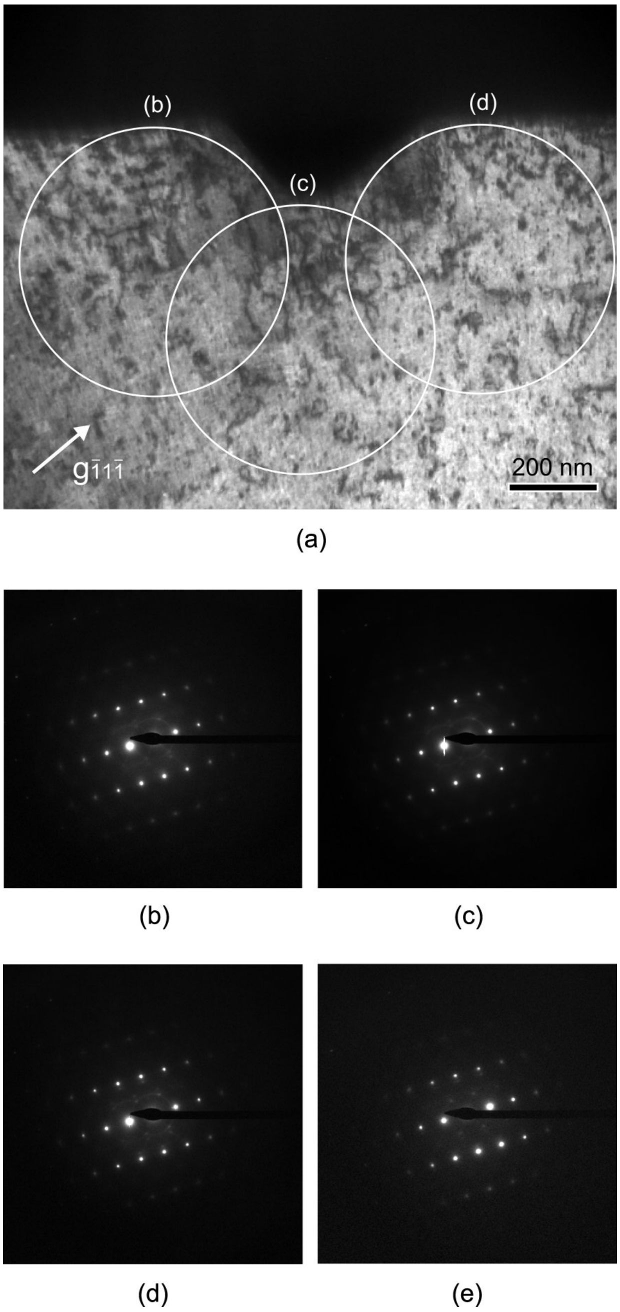

(a)

(b) (c)

(d) (e)

Figure B.3: (a) TEM micrograph of a 0.5 mN indentation taken with a $\bar{1}1\bar{1}$ two beam condition. The white circles mark the positions of the selected area aperture. (b)–(d) Selected area diffraction patterns which correspond to the regions marked in (a). (e) Diffraction pattern of the undeformed crystal far away from the indentation.

Figure B.3 presents the results of the examination in terms of a bright field image as well as the corresponding diffraction images. The circles plotted in the bright field image represent the positions where the selected area aperture was positioned. Comparing the diffraction patterns around the imprint, to the pattern obtained from a dislocation-free region show good agreement. Streaking of the diffraction patterns can not be observed, neither for the region laterally of the indent nor for the region below the indenter tip. This fact supports the occurrence of only slight misorientation gradients.

SAED was also performed on the cross-sectional TEM sample of the 10 mN indentation. The diameter of the used selected area aperture was chosen in such a manner, that the ratio indentation depth–aperture radius was similar for both indentations. The results which look quite different are shown in Figure B.4. Heavy streaking of the diffraction pattern which indicates large orientation changes can be observed, especially on the left-hand side of the indent. The diffraction image of the area below the indenter tip shows pattern-streaking too, but in a somewhat reduced way. Consequently large orientation changes seem to appear only on the left-hand side of the indent and below the indent tip. Streaking on the right-hand side of the indentation is still existent, but diminished.

Another very interesting feature can be observed when comparing the misorientation maps of all performed indentations (see Figure B.1). Starting with the map of the smallest indentation and continuing with the misorientation maps for higher loads, a laterally outwards moving boundary separating pattern I and II is found. It seems that the lateral migration is connected to an accumulation of GNDs at the boundary which accommodates the proceeding shape change of the indentation. The increasing load causes more and more dislocations to group in this area, building up the observed "small angle grain boundary"-like dislocation arrangement. Support for this assumption comes from the fact that the boundary which separates pattern I and II is getting sharper with increasing indentation depth (Figure 1 (a) and (b)). Further confirmation for the observed behavior is given by the examined TEM samples. The "boundary" on the left-hand side of the 0.5 mN indentation which consists of only few dislocations (white ellipse in Figure B.2 (d)) seems to migrate laterally outwards and culminates in the observed sharp boundary for the 10 mN imprint (Figure B.2 (a)). The found phenomenon of moving "grain boundary"-like structures is similar to the deformation-induced migration of grain boundaries in submicrometer-grained films, where mobile boundaries displaced under an in-situ nanoindenter lead to strain-induced coarsening of the microstructure.[11–13]

B.4 Summary and conclusions

In order to characterize the deformation-induced zone below nanoindentations, cross-sectional EBSD and TEM samples were examined. Since EBSD technique is associated with resolutional restrictions especially at very small scan sizes, the deformation-induced zone determined by means of EBSD technique is compared to that obtained

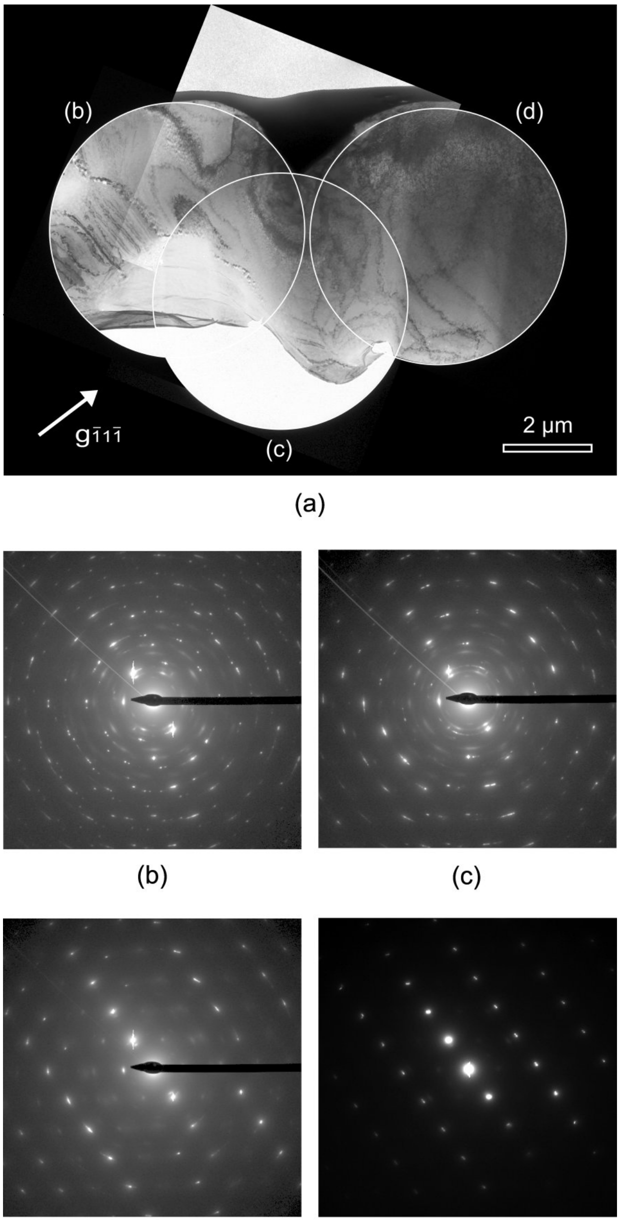

(a)

(b) (c)

(d) (e)

Figure B.4: (a) TEM micrograph of a 10 mN indentation taken with a $\bar{1}1\bar{1}$ two beam condition. The white circles mark the positions of the selected area aperture. (b)–(d) Selected area diffraction patterns which correspond to the regions marked in (a). (e) Diffraction pattern of the undeformed crystal far away from the indentation.

by TEM. Even for shallow indentations good agreement between both methods was found. Analyzing the findings, revealed for large indentations a deformed volume consisting of highly confined deformation-induced patterns while for shallow imprints the found patterns are ambiguous. Additionally performed SAED shows large misorientation gradients beneath the deep imprint and only small gradients near the shallow indentation. This fact was surprising, since for small indentations a very high misorientation gradient was expected. As it seems, the GNDs move far into the bulk, resulting in an only small misorientation gradient. A further interesting finding, similar to deformation-induced grain boundary migration, is a characteristic arrangement of GNDs moving laterally outwards as the load is increased.

Bibliography to paper B

[1] Gane N, Cox JM. Philos Mag 1970;22:881.

[2] Pethica JB, Hutchings R, Oliver WC. Philos Mag A 1983;48:593.

[3] Ma Q, Clark DR. J Mater Res 1995;10:853.

[4] Nix WD, Gao H. Mech Phys Solids 1998;46:411.

[5] Chiu YL, Ngan AHW. Acta Mater 2002;50:2677.

[6] Minor AM, Lilleodden ET, Stach EA, Morris Jr JW. J Mater Res 2004;19:176.

[7] Kiener D, Pippan R, Motz C, Kreuzer H. Acta Mater 2006;54:2801.

[8] Rester M, Motz C, Pippan R. Acta Mater 2007;55:6427.

[9] Maitland T, Sitzman S. Electron backscatter diffraction (EBSD) technique and materials characterization examples. In: Zhou W, Wang ZL, editors. Scanning Microscopy for Nanotechnology – Techniques and Applications. Berlin: Springer, 2007. p.41.

[10] Kiener D, Motz C, Rester M, Jenko M, Dehm G. Mater Sci Eng A 2007;459:262.

[11] Jin M, Minor AM, Stach EA, Morris Jr JW. Acta Mater 2004;52:5381.

[12] Morris JW, Jin M, Minor AM. Mater Sci Eng A 2007;462:412.

[13] Jin M, Minor AM, Morris Jr JW. Thin Solid Films 2007;515:3202.

C

Where are the geometrically necessary dislocations at small indentations?

M. Rester, C. Motz and R. Pippan

Erich Schmid Institute of Materials Science, Austrian Academy of Sciences,
A–8700 Leoben, Austria

Abstract

Electron backscatter diffraction (EBSD) and transmission electron microscopy (TEM) experiments seem to indicate, that small indentations are accommodated by far-reaching dislocation loops inducing only slight misorientation gradients. These low misorientation gradients are only hard to detect and consequently a confirmation of this assumption is up to now not delivered. Using EBSD and TEM technique this work makes an attempt to visualize the far-propagating dislocations by introducing a twin boundary in the vicinity of small indentations. Since dislocations piled up at the twin boundary produce a misorientation gradient, the otherwise far-propagating dislocations can be detected.

C.1 Introduction

During indentation, the indenter causes a permanent plastic imprint on the originally flat material surface. Consequently, the material originally occupying the region of the plastic indent has to be pushed into the underneath substrate.[1] The required material transport is thereby typically performed by defects, e.g. dislocations, which are geometrically necessary.[2] It was found that the density of these so-called geometrically necessary dislocations (GNDs) is proportional to the gradient of plastic strain.[3,4] The concept of GNDs was used by many authors in order to explain the depth dependence of hardness.[5–9] The most prominent approach using geometrically necessary dislocations is those proposed by Nix and Gao.[9] In their mechanism-based model they assumed, that GNDs which accommodate the plastic strain caused by the indenter, are contained in an approximately hemispherical volume below the imprint. The density of GNDs distributed in the hemisphere is thereby found to be proportional to the reciprocal indentation depth. Consequently, at small indentation depths the GND-density as well as the occurring strain gradient becomes very large. However, in reality such high strain gradients can not be observed in metals. As electron backscatter diffraction (EBSD)[10,11] and transmission electron microscopy (TEM)[12–14] experiments show, the plastically deformed zone consists of far-reaching dislocation loops inducing an only slight strain gradient. Similar results were found in in-situ TEM nanoindentation experiments, where the nucleated dislocations are spread over a large volume in the bulk.[15]

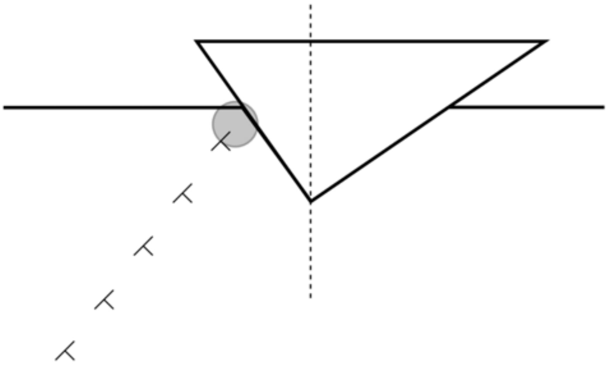

Figure C.1: Dislocation model describing the indentation process of small indentations. The grey area indicates a region where dislocation generation preferably takes place.

An appropriate dislocation model which accounts for the experimental findings and explains the ISE for small indentations, was proposed by Rester et al.[10] (see Figure C.1). In the suggested model, dislocations emitted preferentially at surface defects (e.g. fractured oxide layers) form kinds of prismatic loops which move on slip planes that are arranged very close to each other. As a consequence, the recently generated dislocations have to push the previously created ones towards the bulk material. For very shallow indentations the segment length of the generated dislocations is only small and the stress necessary to push the dislocations away from the indenter is pretty high. Increasing the indentation depth and consequently the segment length of the dislocations causes the observed decrease of the hardness. Such an arrangement induces only slight orientation changes which is in good agreement with the experimental observations.

However, up to now no clear experimental proof for the proposed model is delivered. Since the recently emitted dislocations push the previously ones towards the bulk material, the suggested model can be interpreted as a kind of dislocation avalanche mechanism. Consequently, introducing a barrier would pile-up the dislocations and result in increased misorientation and hardness values. This paper makes an attempt to confirm these statements by investigating the plastically deformed zone of nanoindentations in the vicinity of a twin boundary, and by studying the hardness values in the proximity of such a barrier.

C.2 Experimental

Several indentations with loads of 2.5 mN and 1 mN, respectively, were made in the vicinity of a copper twin boundary using a Hysitron Triboscope fitted with a cube corner indenter (see Figure C.2). Prior to indentation, the specimen was wet ground and mechanically polished using alumina suspension with a grain size of 1 μm. To remove any deformation layer produced during mechanical polishing, the sample surfaces was also electropolished. A focused ion beam (FIB) workstation (LEO 1540 XB) was used to fabricate cross-sections through the center of the indentations. The surface normal of the grain which contains the created indentations was $[\bar{1}4\bar{5}]$, the crystallographic direction parallel to the investigated cross-sections was $[\bar{1}11]$ (see Figure C.2). Consequently all of the fabricated cross-sections belong to the $\{\bar{3}\bar{2}\bar{1}\}$ plane family. In order to protect the imprints against Ga^+ ion damage, the indentations were covered by a 500 nm thick tungsten layer. Before depositing the protection layer, the center of the indentation was marked in order to get the cross-section right through the middle of the indent.[10] Using milling currents of 10 nA, 500 pA and 200 pA, respectively, the material in front of the indentations was removed. On the readily polished cross-sections EBSD investigations were performed using a field emission SEM (LEO 1525) equipped with an EDAX EBSD system. Information on limitations of the EBSD technique and details concerning the used parameters can be found in.[10,16] In a similar way, cross-sections through nanoindentations in copper {111} single crystals made at loads of 2.5 mN and 1 mN, respectively, were fabricated, analyzed and compared to the results found for the indentations in the proximity of the twin boundary.

To gain information about the formed dislocation structures, in addition TEM investigations of the deformation zone were performed. For this purpose, cross-

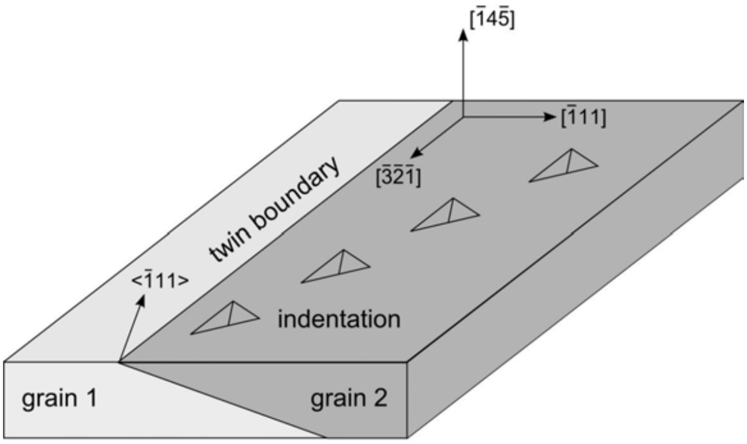

Figure C.2: Schematic illustration showing indents placed in the vicinity of a twin boundary. The plotted crystal directions indicate the orientation of "grain 2".

sectional TEM samples through a 0.5 mN indent placed in the proximity of a twin boundary, and an imprint made in a single crystal, were prepared. Using the FIB workstation, the center of the imprint was marked and a protection layer deposited. Subsequently, two trenches on each side of the imprint were cut which resulted in an approximately 2 μm thick foil containing the indentation. A micromanipulator was used to lift out the foil and to fix it to a TEM sample holder. In a next step, the foil was thinned to electron transparency using acceleration voltages of 30 kV and 5 kV, respectively. All TEM investigations were performed by means of a Philips CM12 TEM operating at 120 kV.

The Hysitron TriboScope was also used to measure the hardness with respect to the distance from the twin boundary. For all indentations the azimuthally orientation of the cube corner indenter was chosen in that way, to have one side of the impression parallel to the twin boundary. To avoid overlapping of the plastically deformed zones, the indents were performed with a sufficient offset (see Figure C.2). The indentations were all made in load-controlled mode, applying a force of 200 μN.

C.3 Comparison – Single crystal and twin

The results of the EBSD study for both, the indentations in the proximity of the twin boundary and those in the single crystal, are presented in terms of misorientation maps in Figure C.3. Starting with the misorientation map of the 2.5 mN indentation, performed in single crystalline copper (Figure C.3 (a)), a far-reaching deformation-induced zone can be observed. On the left-hand side, where the imprint is cut through the face of the indentation, the misoriented volume is fragmented and extends laterally to a distance of approximately 1.5 times the indent diameter. Axially the plastically deformed zone reaches deep into the bulk, far beyond the imprints residual depth. The misoriented volume on the right-hand side of the indentation, however, looks quite different. Only directly beneath the indentation flank a mentionable misorientation of the material can be found.

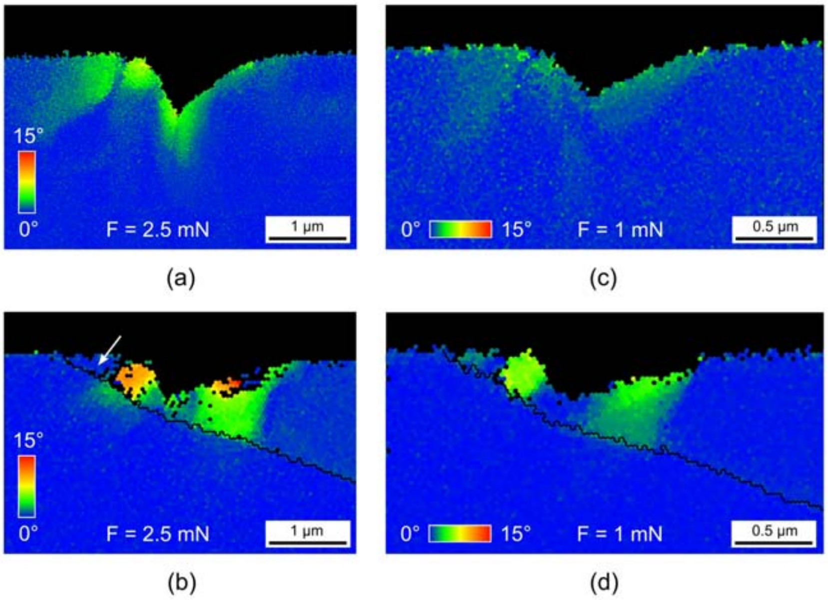

Figure C.3: Misorientation maps of cross-sections through imprints in copper for loads of 2.5 mN and 1 mN. The imprints in (a) and (c) were performed in {111} single crystals, while the indentations in (b) and (d) were made in the vicinity of a twin boundary.

But what happens to the deformation-induced zone if a barrier, as e.g. a twin boundary, is introduced? The answer is delivered by Figure C.3 (b), where the misorientation map of a 2.5 mN imprint in the vicinity of a twin boundary is presented. At the left hand-side of the imprint, where in the single crystalline case a far-reaching deformation pattern appears, a strongly confined misorientation pattern is observed. It can be seen, that the misoriented volume extends beyond the twin boundary, building up a small area with only minor misorientation. Very interesting is the triangular area left of the indent, between sample surface and twin boundary, where no misorientation appears (indicated by the arrow in Figure C.3 (b)). This fact is rather surprising, since the large lateral expansion of the plastically deformed zone observed in the single crystalline case, may expect a high misorientation in this triangular region. As it seems, the twin boundary prevents the formation of misoriented volume in this area. Examining the right-hand side of the imprint shows a deformation-induced pattern with an almost homogeneous orientation distribution. Only directly beneath the indent flank the misorientation is increased. This fact is in contrast to the deformation-induced pattern found for the single crystal imprint (Figure C.3 (a)), where on the right-hand side almost no misoriented volume appears. It seems that the twin boundary piles up the emitted dislocations producing the observed misorientation pattern, while in the single crystal the dislocations propagate far into the bulk and induce an only slight misorientation gradient.

The consequences associated with a reduction of the applied load, are presented in Figure C.3 (c). For the single crystalline case, the deformation zone of the 1 mN indent is similar to those of the 2.5 mN imprint (cp. Figure C.3 (a)). The main differences are a much lower misorientation as well as less defined deformation-induced patterns. Introducing a twin boundary yields to the misorientation map, presented in Figure C.3 (d). Similar to the 2.5 mN imprint (cp. Figure C.3 (b)) here as well significant misorientations, created by piled up GNDs, appear.

The results of the additionally performed TEM investigations are presented in Figure C.4 (a) and (b). As can be seen, the misoriented volume of the imprint in single crystalline copper (Figure C.4 (a)) consists of individual dislocation loops surrounding the imprint. Below the indent tip, a slightly higher dislocation density occurs, but neither dislocation pile-ups nor dislocation cells are observed. A completely different picture is found for the imprint in the vicinity of the twin boundary, shown in Figure C.4 (b). Noticeable is a very dense dislocation network on the left-hand side of the imprint tip. It seems that dislocations, which in the singly crystalline case move into the bulk, are now piled up in front of the twin boundary. Besides the dense dislocation network, on the other hand, dislocation-free zones appear. On the right-hand side of the indent the dislocations are distributed more uniformly, building up a dislocation arrangement of only moderate density. It has to be noticed, that dislocation decoration of the twin boundary appears not only in the region where the dense dislocation arrangement adjoins. Those parts of the boundary, which are far away from the dislocation networks, show a decoration of dislocations as well. This observation supports the fact of far-propagating dislocations, provided that no obstacles are present.

C.4 Hardness in the proximity of a twin boundary

Summing up the results of the EBSD and TEM experiments show, that the twin boundary piles up dislocations which in the single crystalline case propagate far into the bulk. It is well known, that piled up dislocations produce a large back stress and thus impede the generation of further dislocations. As a consequence, the hardness in the vicinity of a barrier, e.g. a twin boundary, should be increased. Figure C.5 shows a graph, were the hardness is plotted as a function of the distance to the twin boundary. As can be seen, the hardness drops from approximately 1.4 GPa directly beneath the twin boundary to a value of 1.25 GPa far away from the boundary. Also included in the diagram are the hardness values of an $\{111\}$ and an $\{100\}$ oriented single crystal, whereas the hardness of the $\{\bar{1}4\bar{5}\}$ oriented grain is found in-between. These findings further support the existence of a pile-up based dislocation model explaining the accommodation of small imprints.

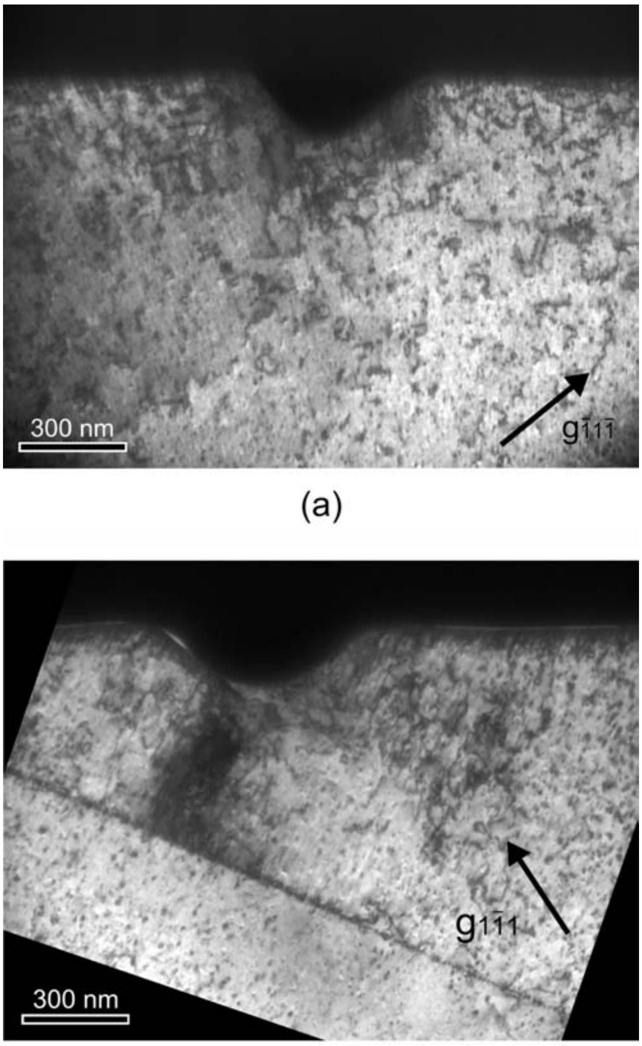

(a)

(b)

Figure C.4: Cross-sectional TEM micrographs of 0.5 mN indentations in copper, taken with a $\bar{1}1\bar{1}$ two beam condition (a) and a $1\bar{1}1$ two beam condition, respectively. The indentation in (a) was performed in a $\{111\}$ single crystals, while the indentations in (b) was made in the vicinity of a twin boundary.

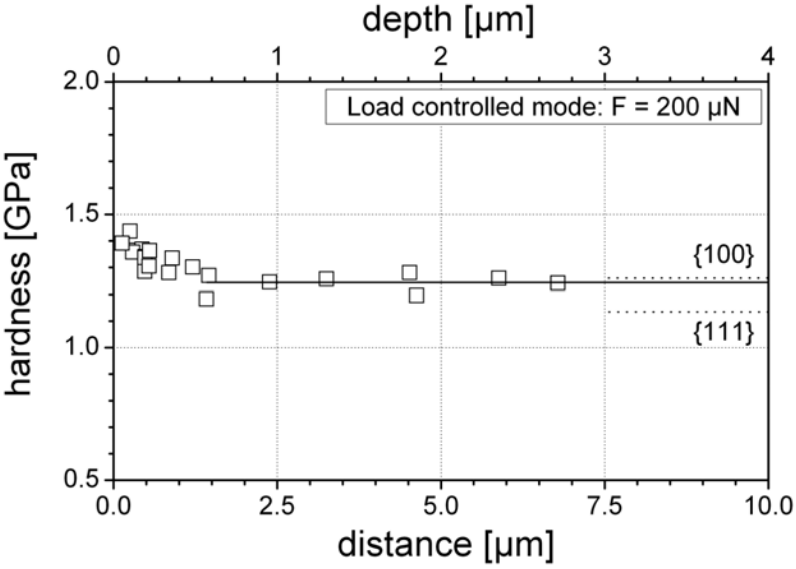

Figure C.5: Hardness as a function of the lateral (bottom) and the axial (top) distance to the twin boundary. All indentations were performed in "grain 2" (see Figure C.2) under load controlled mode applying a force of 200 μN. Also plotted is the hardness of {100} and {111} single crystalline copper.

C.5 Summary and conclusions

In summary, the experimental findings corroborates that small indentations are governed by dislocation generation and the back-stress of dislocations pushed into the bulk. Facts which support the suggested model are:

- The proposed dislocation arrangement for very small indentations induces only slight misorientation gradients, which is in accordance to the experimental observations (see Figure C.3 (a) and (c))

- Introducing a barrier leads to a pile-up of dislocations (see Figure C.4 (b)) and consequently to increased misorientation (see Figure C.3 (b) and (d)).

- Formed pile-ups induce a back-stress which impedes further dislocation generation. The result is an increase of hardness in the proximity of the barrier (see Figure C.5).

- Discrete dislocation simulations show that small indentations are accommodated by far-reaching dislocation loops, which induce an only slight misorientation gradient.[17–19]

Of course the suggest dislocation model is a simplified one and it does not take into account the slip geometry and the complex three-dimensional dislocation arrangement; but nevertheless it describes many of the experimental findings in a very good manner.

Bibliography to paper C

[1] Gao H, Huang Y. Scripta Mater 2003;48:113.

[2] Cottrell AH. The Mechanical Properties of Matter. New York: Wiley; 1964.

[3] Nye JF. Acta Metall 1953;1:153.

[4] Ashby MF. Philos Mag 1970;21:399.

[5] Stelmashenko NA, Walls MG, Brown LM, Milman YV. Acta Metall Mater 1993;41:2855.

[6] De Guzman MS, Neubauer G, Flinn P, Nix WD. Mater Res Symp Proc 1993;308:613.

[7] Fleck NA, Muller GM, Ashby MF, Hutchinson JW. Acta Metall Mater 1994;42:475.

[8] Ma Q, Clarke DR. J Mater Res 1995;10:853.

[9] Nix WD, Gao H. J Mech Phys Solids 1998;46:411.

[10] Rester M, Motz C, Pippan R. Acta Mater 2007;55:6427.

[11] Rester M, Motz C, Pippan R. Mater Res Soc Symp Proc 2007;1049:AA03-03.

[12] Chiu YL, Ngan AHW. Acta Mater 2002;50:2677.

[13] Wo PC, Ngan AHW, Chiu YL. Scripta Mater 2006;55:557.

[14] Wo PC, Ngan AHW, Chiu YL. Scripta Mater 2007;56:323.

[15] Minor AM, Asif SAS, Shan Z, Stach EA, Cyrankowski E, Wyrobek TJ, Warren OL. Nature Mater 2006;5:697.

[16] Kiener D, Pippan R, Motz C, Kreuzer H. Acta Mater 2006;54:2801.

[17] Balint DS, Deshpande VS, Needleman A, Van der Giessen E. J Mech Phys Solids 2006;54:2281.

[18] Kreuzer HGM, Pippan R. Acta Mater 2007;55:3229.

[19] Nicola L, Bower AF, Kim KS, Needleman A, Van der Giessen E. J Mech Phys Solids 2007;55:1120.

D

Microstructural investigation of the deformation zone below nano-indents in copper

M. Rester, C. Motz and R. Pippan

Erich Schmid Institute of Materials Science, Austrian Academy of Sciences,
A–8700 Leoben, Austria

Abstract

The deformation zone below nanoindents in copper single crystals with an $\langle 1\bar{1}0\rangle$ $\{111\}$ orientation is investigated. Using a focused ion beam (FIB) system, cross-sections through the center of the indents were fabricated and subsequently analyzed by means of electron backscatter diffraction (EBSD) technique. Additionally, cross-sectional TEM foils were prepared and examined. Due to changes in the crystal orientation around and beneath the indentations, the plastically deformed zone can be visualized and related to the measured hardness values. Furthermore, the hardness data were analyzed using the Nix-Gao model where a linear relationship was found for H^2 vs. $1/h_c$, but with different slopes for large and shallow indentations. The measured orientation maps indicate that this behavior is presumably caused by a change in the deformation mechanism. On the basis of possible dislocation arrangements, two models are suggested and compared to the experimental findings. The model presented for large imprints is based on dislocation pile-up's similar to the Hall-Petch effect, while the model for shallow indentations uses far-reaching dislocation loops to accommodate the shape change of the imprint.

D.1 Introduction

It is well known for many years that the hardness of metals and alloys in the micron and sub-micron regime is not a constant number. In fact the hardness depends on the size of the indent i.e., with decreasing indentation depth the hardness increases.[1–3] This is called the indentation size effect (ISE). Using the concept of geometrically necessary dislocations (GNDs) and the Taylor rule for the flow stress, Nix and Gao (N-G) proposed a model to explain the ISE.[4] According to this model, a linear correlation between H^2, the square of the hardness, and $1/h_c$, the reciprocal indentation depth exists, which is in good agreement with micro-indentation hardness data. In the literature, however, it is reported that nanoindentation hardness data do not follow this linear trend over the whole measurement range.[5–7] Instead, at small indentation depths they start to deviate from the predicted linear curve. In order to verify if this behavior is linked to a change in the deformation structure the plastically deformed volume below different sized nanoindentations is visualized using electron backscatter diffraction (EBSD) and transmission electron microscopy (TEM). The results were subsequently used to suggest possible dislocation arrangements in order to explain the indentation process of large and shallow imprints.

D.2 Experimental

Copper single crystals with an $\langle 1\bar{1}0 \rangle \{111\}$ orientation were prepared by wet grinding and mechanical polishing. Electropolishing was subsequently performed on the $\{111\}$ surface in order to remove any deformation layer produced during previous polishing steps. Using a Hysitron TriboScope fitted with a cube corner indenter the hardness and the indentation modulus of the material at loads between 40 μN and 10 mN were determined. A calibrated area function was obtained using a procedure outlined by Oliver and Pharr.[8] For all indentations the load function described in[9] was used. The presented results are an average of three to five indentations of each selected indenter load.

Cross-sections through the imprints were produced using a LEO 1540 XB focused ion beam (FIB) workstation. For this purpose, several indentations with loads between 0.5 mN to 10 mN were produced in the vicinity of a carefully mechanically polished edge. To protect the imprints against Ga^+ ion damage a 500 nm thick tungsten layer was deposited over the indents. Prior to depositing, the center of the indents were marked in order to get the cross-sections right through the middle of the indents. Using milling currents of 10 nA, 500 pA and 200 pA, respectively, the material in front of the indents was removed. On the readily polished cross-sections EBSD investigations were performed using a LEO 1525 field emission scanning electron microscope (SEM) equipped with an EDAX EBSD system. Since plastic deformation is usually associated with crystal orientation changes, traces of the plastic deformation can be visualized.

TEM samples were also prepared using the FIB workstation. Indents with loads between 500 μN and 10 mN were made and protection layers were deposited. By cutting two trenches on each side of the indents, a foil with a thickness of approximately 2 μm was fabricated. After lifting out, the foil was thinned to electron transparency using acceleration voltages of 30 kV and 5 kV, respectively. All TEM examinations were performed using a Philips CM12 TEM operating at 120 kV.

D.3 Results and discussion

The results of the hardness measurement obtained for the {111} surface of copper are presented in Figure D.1. As can be seen, the hardness data show a pronounced ISE. Starting at a value of 2.75 GPa the hardness decreases to 1.1 GPa at a depth of 1.8 μm. The reduced indentation modulus is over the whole measuring range on a rather constant level of approximately 125 GPa.

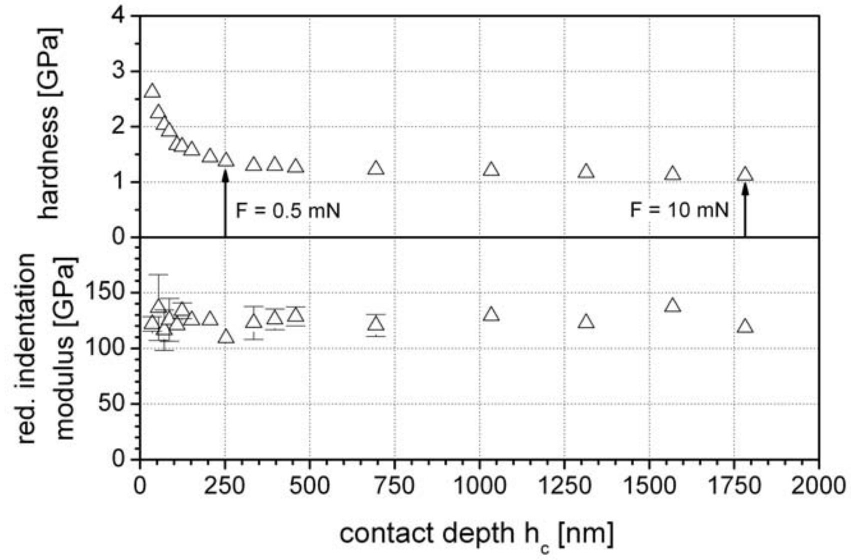

Figure D.1: Hardness and reduced indentation modulus as a function of the contact depth. The hardness values of the largest and the smallest microstructurally investigated imprints are marked by arrows.

In order to verify if the Nix-Gao model fits the hardness data, the square of the hardness is plotted against the reciprocal indentation depth. The resulting plot is displayed in Figure D.2, with an inset showing the hardness data for depths greater 100 nm enlarged. What can be observed is a hardness curve which consists of two linear regimes. Regime α thereby extends from the largest indentation depth to a depth of about 1 μm, whereas regime β describes the hardness for imprints smaller than 1 μm. This is somewhat different to the results found in literature, where the hardness data at small indentation depths starts to deviate in a non-linear way.[5–7]

To find an explanation for the observed bi-linear behavior, the microstructure of

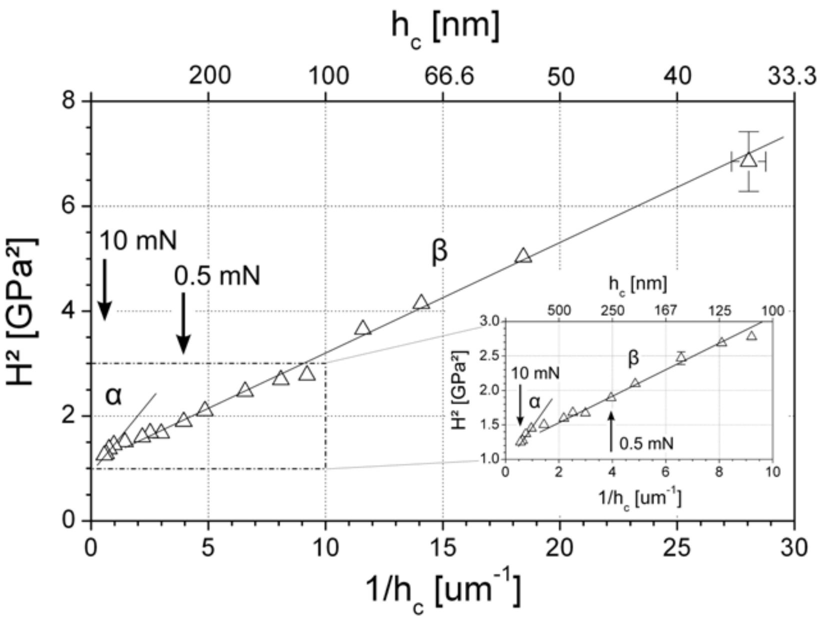

Figure D.2: Application of the Nix-Gao model to the measured hardness values. The inset shows the hardness data for depths greater than 100 nm enlarged. The arrows mark the largest and the smallest of the microstructurally examined indentations.

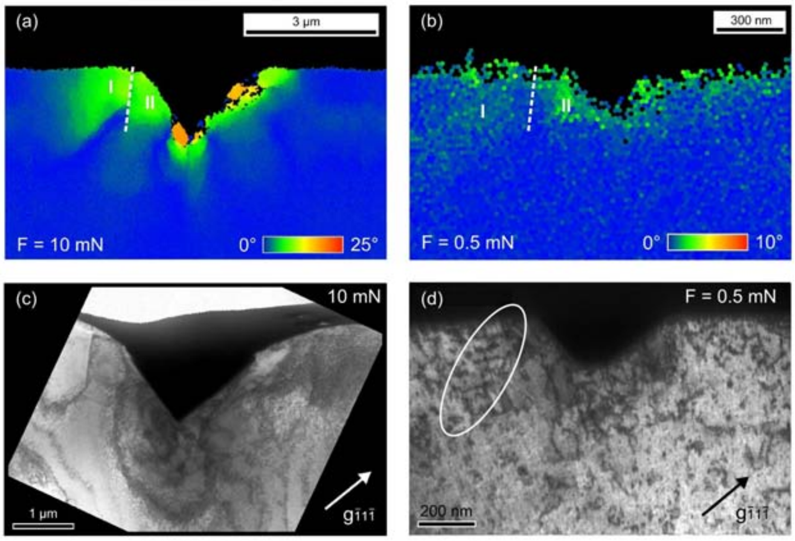

Figure D.3: Misorientation maps (a)–(b) and TEM micrographs (c)–(d) for a 10 mN and a 0.5 mN indent in copper {111} single crystals. The TEM micrographs were taken with a $\bar{1}1\bar{1}$ two beam condition.

the deformation-induced zone below nanoindentations was investigated by means of EBSD and TEM technique. The results of the EBSD and TEM studies for a 10 mN and a 0.5 mN indent are shown in Figure D.3 (a)–(d). Starting with the misorientation map of the large indent (a), on the left hand side two deformation-induced rotation patterns (I and II), which are separated by a boundary, can be found. Another interesting part is the region below the indenter tip, where a kind of sub-grain formation occurs. Both characteristic features can be found as well in the TEM micrograph as illustrated in Figure D.3 (c). However, the deformation-induced zone of the small imprint looks somewhat different. A pronounced boundary as found for the 10 mN indent can not be observed. Rather, pattern I and II are separated by a only less defined boundary (Figure D.3 (b)). This fact is confirmed by the TEM micrograph where instead of a sharp boundary, single dislocations appear (the region is marked by the white ellipse in Figure D.3 (d)). Both the bi-linear behavior of the hardness data (Figure D.2) as well as the results obtained from the EBSD and TEM studies indicate a change in the deformation mechanism.

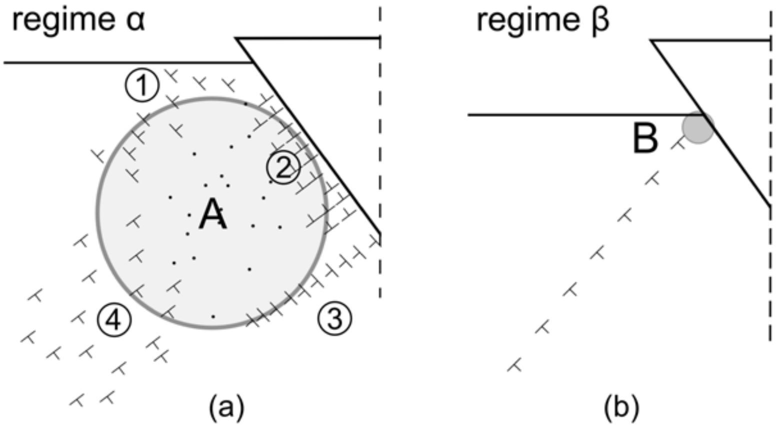

Figure D.4: Dislocation models describing the indentation process of large (a) and shallow (b) imprints.[9]

In order to explain the observed behavior, possible arrangements of GNDs reflecting the characteristic features are presented in Figure D.4. For large indentations a pile-up model similar to those used to describe the Hall-Petch relation is suggested. Since large indentations are always accompanied by the occurrence of a huge and far-reaching shear stress field, dislocation sources located near the indenter flank (region A in Figure D.4 (a)) can be activated and are able to emit dislocation loops. To simplify matters, only two types of slip planes, one perpendicular to the indenter flank and the other parallel to it, are assumed to generate dislocations. Dislocation loops emitted on slip planes perpendicular to the indenter flank start to move towards the indenter and pile up in front of the indenter, producing the required large orientation changes (region 2). This results in a pile-up inducing a significant back stress to the sources and impedes further dislocation generation. Dislocations with an opposite sign move into the opposite direction towards the bulk material (region 4) and arrange there in a very widespread manner. Consequently, the induced orientation gradient is only small. Dislocation loops generated on the slip planes parallel to the indenter flank move into the region below the indenter tip. However, due to a change in the shear stress field they are not able to overcome the center region. Instead they form a pile up at the "symmetry" line (region 3). The other parts of the loops move towards the free surface where few of them exit the material. But the majority of the dislocations arrange themselves in the region where the shear stress goes to zero, forming the observed boundary (region 1).

But why does the described mechanism become less important when the indentation depth is decreased? Lowering the indentation depth is directly linked to a diminishment of region A and consequently to a decrease of the number of dislocation sources which can be activated. This results in an increase of the back stress originating from the dislocations piled up in region 2 and 3. As a result, the generation of further dislocations is impeded. Due to the hindered dislocation emission, other mechanisms like dislocation generation laterally of the indent become more important. The emitted dislocations form kinds of prismatic loops, which move on slip planes arranged very close to each other. As a consequence, the recent generated dislocations have to push the previously created ones towards the bulk material. However, for extremely shallow indents the segment length of the dislocations generated in region B becomes very small and therefore the stress required to push the dislocations away from the indenter flank is very high. Increasing the indentation depth and thus the segment length of the dislocations causes the observed decrease of hardness.

To verify if the suggested models are realistic, the required shear stress to obtain such a dislocation arrangement is estimated. To convert the received stress into hardness, Tabors rule was used.[10] For large indentations the pile-up model described in Figure D.4 (a) seems to be responsible for the ISE. Since there are similarities to the Hall-Petch (H-P) effect, the H-P relation

$$\tau_\alpha = \tau_{HP} = \tau_0 + \frac{k'_{HP}}{\sqrt{h_c}} \tag{D.1}$$

is used to calculate the shear stress for regime α.[11,12] The grain size thereby is substituted by the indentation depth h_c which is in turn proportional to the size of region A, and τ_0 and k'_{HP} are constants. However, since the kink in the N-G plot (Figure D.2) refers to a change in the deformation mechanism this type of stress calculation is only valid for regime α. For regime β, the stress is estimated in a different way. As can be seen in the dislocation model presented for shallow nanoindentations (Figure D.4 (b)), single dislocation events become more and more important. As a consequence, the size of dislocation sources as well as the back stress originating from previous emitted dislocations has to be considered for stress calculation as well.[13–15] Thus, the following relation can be found

$$\tau_\beta = \tau_{source} + \tau_{back} = \frac{Gb}{2\pi s} ln\left(\frac{\alpha s}{b}\right) + \frac{Gb}{2\pi^2 D} ln\left(\frac{\sqrt{2}h_c}{b}\right) \tag{D.2}$$

Here G is the polycrystalline shear modulus, b is the Burgers vector of copper, s the source size which was assumed to be $2h_c$ and α a numerical constant in the order of unity. D, the diameter of the area where dislocations were emitted is assumed to be 150 nm. Converting the calculated stress into hardness values and plotting them in the N-G plot shows good agreement (Figure D.5).

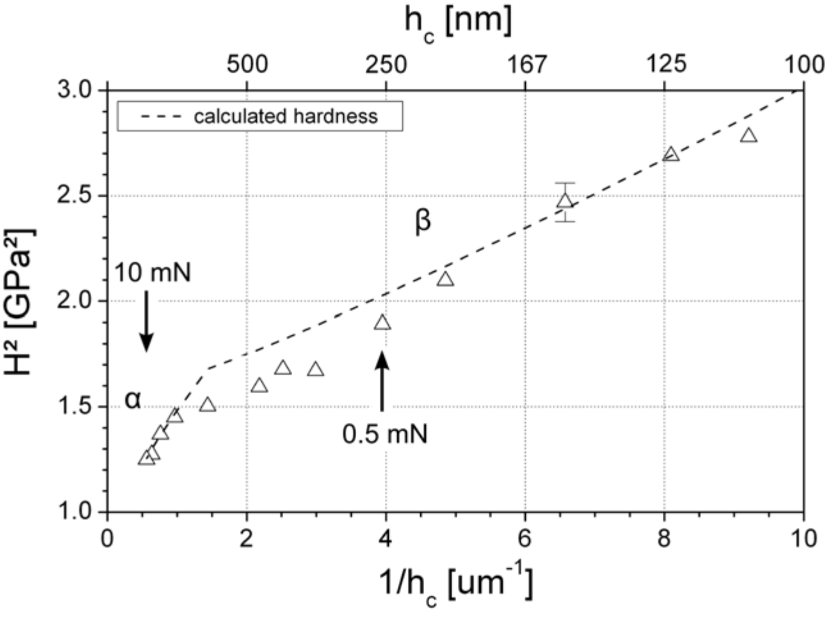

Figure D.5: Comparison of the measured hardness data to the calculated hardness for depths up to 100 nm using a Nix-Gao plot. The arrows mark the largest and the smallest of the examined indentations.

Special attention was paid to the fact that the used values for s, the source size and D, the diameter of the region where dislocation emission takes place are plausible. Even though the performed calculations are only rough estimations, they nevertheless demonstrate that the supposed dislocation models are able to describe the observed bi-linear behavior of the hardness data.

D.4 Conclusions

Studying the N-G plot of the hardness data measured on {111} copper single crystals reveals two linear regimes, one for indents with depths greater 1 μm and one for indents smaller than 1 μm. It is assumed that this bi-linearity is linked to a change in the deformation mechanism. EBSD and TEM studies, performed for a large and a shallow indent support this assumption. On the basis of the experimental findings two models of possible dislocation arrangements are presented and used to explain the ISE. Subsequently, the shear stress field of the dislocation arrangements was estimated and by means of Tabors rule compared to the measured hardness data. The hardness values of the simple estimation show good agreement with the experimental findings.

Bibliography to paper D

[1] Gane N, Cox JM. Philos Mag A 1970;22:881.

[2] Pethica JB, Hutchings R, Oliver WC. Philos Mag A 1983;48:593.

[3] Ma Q, Clark DR. J Mater Res 1995;10:853.

[4] Nix WD, Gao H. J Mech Phys Solids 1998;46:411.

[5] Lim YY, Chaudhri MM. Philos Mag A 199;79:2979.

[6] Swadener JG, George EP, Pharr GM. J Mech Phys Solids 2002;50:681.

[7] Feng G, Nix WD. Scripta Mater 2004;51:599.

[8] Oliver WC, Pharr GM. J Mater Res 1992;7:1564.

[9] Rester M, Motz C, Pippan R. Acta Mater 2007;55:6427.

[10] Tabor D. Proc R Soc A 1947;192:247.

[11] Hall EO. Proc Phys Soc B 1951;64:747.

[12] Petch NJ. J Iron Steel Inst 1953;174:25.

[13] Fisher JC, Hart EW, Pry RH. Phys Rev 1952;87:958.

[14] Friedman LH, Chrzan DC. Philos Mag A 1998;77:1185.

[15] von Blanckenhagen B, Arzt E, Gumbsch P. Acta Mater 2004;52:773.

E

Stacking fault energy and indentation size effect: Do they interact?

M. Rester, C. Motz and R. Pippan

Erich Schmid Institute of Materials Science, Austrian Academy of Sciences,
A–8700 Leoben, Austria

Abstract

To investigate the influence of the stacking fault energy (SFE) on the indentation size effect (ISE), nanoindentation was performed on silver, copper and nickel with small, intermediate and high SFE. Additionally, to analyze the impact of the SFE on the developed misorientation of the crystal, electron backscatter diffraction was performed on cross-sections fabricated through imprints of the different metals. In both experiments no evidence was found that the SFE influences the ISE or the deformation patterns below the indents.

The stacking fault energy (SFE) plays an important role in the deformation of face-centered cubic (fcc) metals,[1–3] because it affects dislocation nucleation, the movement of dislocations and the type of dislocation patterns formed.[4] A low SFE causes a large separation of partial dislocations, whereas in metals with a high SFE the separation is only small.[5] Since pinching of partial dislocations and subsequent cross-slip is an important mechanism during the deformation of fcc metals, the resistance against plastic deformation is linked to the value of the SFE. High SFE facilitates pinching of the dislocation partials and consequently dislocation cross-slip. This results in increased dynamic recovery and a decrease in the hardening rate. In metals with low SFE, on the other hand, the rate and intensity of cross-slip is impeded, which increases the plastic hardening.[6] Furthermore, the dislocation nucleation process in fcc metals is influenced by the SFE as well. Besides emitting perfect dislocation loops, e.g. by means of Frank-Read sources, a very common type of dislocation nucleation is those via Shockley partials.[7,8] Instead of emitting a perfect dislocation, a leading partial dislocation is nucleated and starts to propagate, leaving behind a stacking fault. Soon afterwards a trailing partial follows and arranges in a position equal to the equilibrium splitting distance.[9,10] Since dislocation nucleation, dislocation movement as well as the resulting dislocation patterns are influenced by the value of the SFE, metals with differing SFEs may exhibit differently pronounced indentation size effects (ISEs).

Table E.1: Stacking fault energy γ_{SF}, elastic anisotropy A and reduced indentation modulus E_{red} of different fcc metals at 300 K. γ_{SF} was taken from[11] while the elastic anisotropy was calculated using elastic constants from.[12] E_{red} for the $\{111\}$ surface was calculated by a method proposed by Vlassak and Nix[13] using elastic constants from.[12]

Metal	Ag	Cu	Ni
γ_{SF} [mJ/m^2]	16	40	125
A [-]	2.9	3.2	2.4
E_{red} [GPa]	90	135	203

In order to investigate how the ISE is influenced by varying SFEs, three metals, silver as a metal with low SFE, nickel as a metal with high SFE and copper with an intermediate SFE, were chosen (see Table E.1). The single crystals, all with an $\{111\}$ surface orientation, were wet ground and mechanically polished using alumina suspension with a grain size of 1 μm. Electropolishing was then performed in order to remove any deformation layer produced during the previous polishing steps. Details of the electropolishing techniques used are summarized in Table E.2. Nanoindentations were carried out on the polished $\{111\}$ surface planes at loads between 40 μN and 10 mN. The device used was a Hysitron TriboScope fitted with a cube corner indenter which exhibited a tip radius of approximately 40 nm. To obtain sufficient lattice rotations for the electron backscatter diffraction (EBSD) measurements, especially for very shallow indentations, a cube corner indenter was favored over a Berkovich indenter. The increased indenter-specimen friction associated with the application of a cube corner indenter was accepted for these purposes. However, in order to detect possible errors connected to the hardness measurement using a cube corner indenter, the trends of the acquired indentation moduli were used as a kind of indicator. The load function used for all indentations consisted of a 5 s loading part, a 20 s holding segment at maximum load in order to minimize creep effects and a 17 s unloading part, which included a 10 s holding period at 10% of the peak load. For every selected indenter load three to five separate indentations were made. The presented results are an average of these indentations. The error bars inserted in Figures E.1-E.3 represent the standard deviation of each set of these measurements. The temperature during all experiments was 25 ± 2 ℃. In order to obtain accurate indentation results a calibrated area function for the cube corner indenter as well as a correct value of the machine compliance is required. For these purposes the procedure outlined by Oliver and Pharr was applied.[15]

Table E.2: Parameters used in the electropolishing of silver, copper and nickel samples. For electropolishing of silver, an external power supply unit attached via platinum electrodes was used, while copper and nickel were polished by means of a Struers Polectrol. The material removal for all samples was of the order of 30 μm.

Metal	Ag	Cu	Ni
Electrolyte	[14]	D2	A2
Voltage [V]	9	45	40
Flow-rate	–	3.5	2.5
Duration [s]	90	5	4

The results of the hardness measurement as well as the corresponding modulus values are presented in Figure E.1. As can be observed, all investigated materials show a pronounced ISE. For silver, the metal with the lowest SFE, the hardness curve starts at 1.75 GPa and decreases to a value of 0.7 GPa as the load increases. The hardness curve for copper, however, decreases from a value of 2.75 GPa at a depth of 35 nm to approximately 1.1 GPa for the largest imprint. For nickel, the hardest of the investigated metals, the ISE curve starts at 4 GPa and approaches a hardness plateau of approximately 1.6 GPa. The reduced indentation moduli of all three metals are found to be rather constant over the whole measuring range with 95 GPa for silver, 125 GPa for copper and 190 GPa for nickel. Only the indentation modulus for nickel decreases slightly for depths greater than 1 μm. The observed modulus scatter especially at very small indentation depths can be attributed to thermal drift effects.[16]

In order to illustrate the influence of the SFE on the ISE it is necessary to normalize the hardness curves by an appropriate parameter. For this purpose, all factors influencing the hardness of a metal have to be determined. Using Tabors rule,[17] where the hardness H of a metal is about three times the flow stress σ_y, the following dependency can be found:[18, 19]

$$H = f(\sigma_y) = f(b, \rho, T, \dot{\epsilon}, \mu, \gamma_{SF}) \tag{E.1}$$

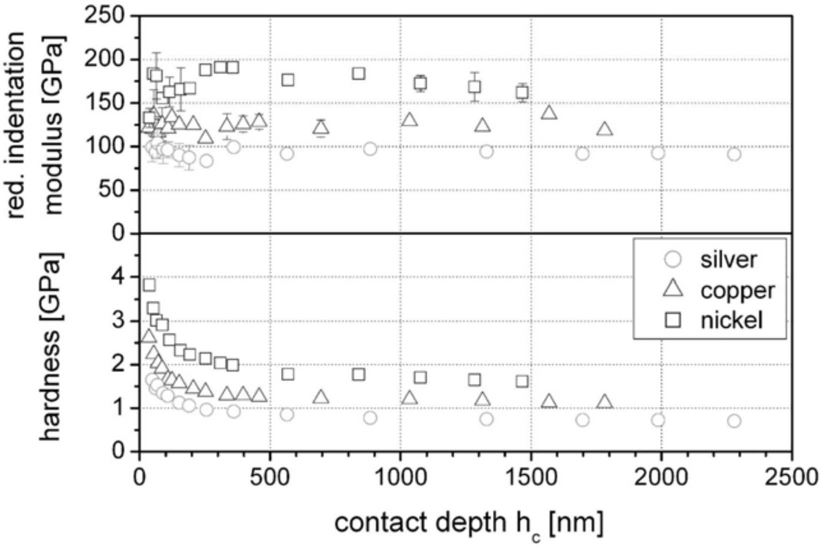

Figure E.1: Hardness and reduced indentation modulus for silver, copper and nickel {111} single crystals as a function of contact depth. The experiments were conducted using a Hysitron TriboScope fitted with a cube corner indenter. Error bars are inserted only for those datum points where the error bar is larger than the size of the symbol.

where b is the Burgers vector, ρ the initial dislocation density, T the temperature, $\dot{\epsilon}$ the strain rate, μ the shear modulus and γ_{SF} the SFE. Considering that the samples used were all single crystals with not very different Burgers vectors and an initial dislocation density of the same order of magnitude, the dependency of Eq. E.1 reduces to T, $\dot{\epsilon}$, μ and γ_{SF}. In addition, all indentation tests were carried out under the same experimental conditions such as a steady temperature T and a constant strain rate $\dot{\epsilon}$. Thus, Eq. E.1 can be rewritten as:

$$H = f(\mu, \gamma_{SF}) \tag{E.2}$$

Analyzing Eq. E.2 shows that all constant factors influencing the hardness were eliminated. Thus, the number of factors affecting the hardness reduces to the shear modulus and the SFE. Since the impact of the SFE on the ISE is to be investigated, the shear modulus seems to be an appropriate parameter to normalize the hardness curves. However, in indentation experiments, the conventional Youngs or shear modulus is typically replaced by the so-called reduced indentation modulus E_{red}. This is due to the fact that the indented materials, which are often single crystalline or textured materials, show strong elastic anisotropy. Values for the elastic anisotropy A of Ag, Cu and Ni can be found in Table E.1. In order to consider the elastic anisotropy, the reduced indentation modulus is used to normalize the hardness curves instead of applying the conventional Youngs or shear modulus. A graph showing the normalized hardness curves is presented in Figure E.2. The applied reduced indentation moduli, calculated by a method proposed by Vlassak and Nix,[13] are listed in Table E.1. Examining Figure E.1 shows that the curves for silver, copper as well as nickel are in very good agreement and no significant differences can be observed. However, since the nucleation and movement of dislocations is controlled by the SFE, great differences between the hardness curves may be expected especially at small indentation depths. To facilitate a more accurate investigation of the curves, particularly at small depths, the normalized hardness was plotted against the reciprocal indentation depth. The results are presented in Figure E.3 and show that the normalized hardness curves for copper and nickel are on top of each other. Only the curve for silver, the metal with the lowest SFE, is slightly higher than those for copper and nickel. Due to these facts it seems that the SFE has no influence on the ISE of fcc metals.

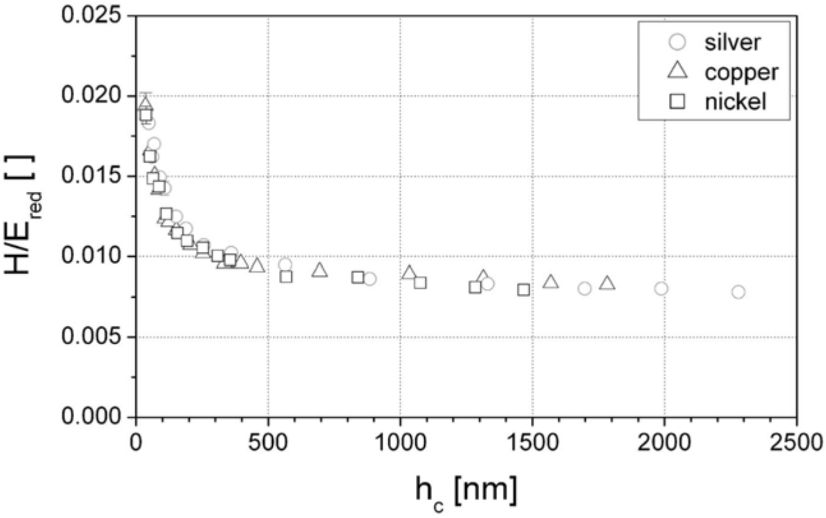

Figure E.2: Normalized hardness for silver, copper and nickel {111} single crystals as a function of contact depth. The hardness values were normalized by the reduced indentation moduli E_{red} calculated after a method proposed by Vlassak and Nix.[13] The used reduced indentation moduli are listed in Table E.1. Error bars are inserted only for those datum points where the error bar is larger than the size of the symbol.

Since dislocation patterns formed during deformation are dependent on the SFE, metals with differing SFEs might show different dislocation arrangements. Therefore, the misorientation and the shape of the regions beneath imprints were examined. For this purpose, cross-sections through the center of imprints made at loads of 1, 2.5, 5 and 10 mN were fabricated and subsequently examined using EBSD.[16,20] Due to changes of the crystal orientation caused by plastic deformation, the geometrically necessary dislocations (GNDs) causing these changes can be visualized. All examined cross-sections were fabricated using a LEO 1540 XB focused ion beam workstation. The EBSD experiments were performed using a LEO 1525 field emis-

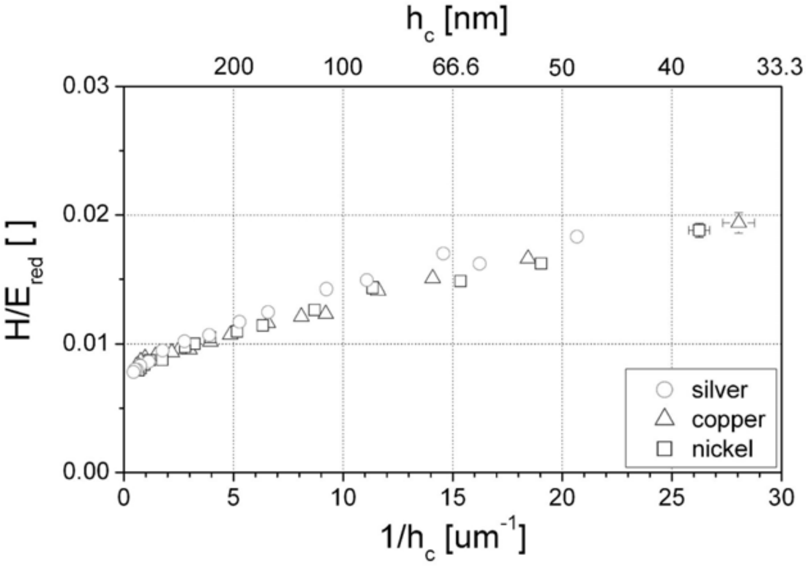

Figure E.3: Normalized hardness curves for silver, copper and nickel {111} single crystals as a function of the reciprocal contact depth. The hardness values were normalized using the reduced indentation moduli E_{red} calculated after a method proposed by Vlassak and Nix.[13] The used reduced indentation moduli are listed in Table E.1. Error bars are inserted only for those datum points where the error bar is larger than the size of the symbol.

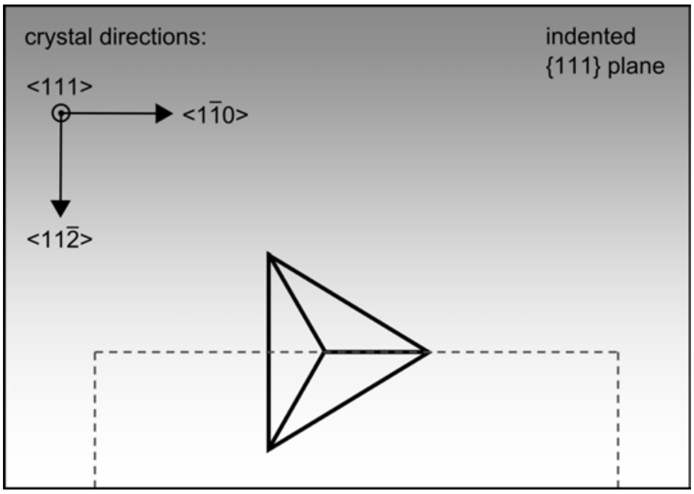

Figure E.4: Schematic diagram showing how the indents were cut as well as the positions of the imprints with respect to the crystal orientation.

sion scanning electron microscope equipped with an EDAX EBSD system. A sketch showing how the indents were cut as well as the positions of the imprints with respect to the crystal orientation is presented in Figure E.4. In the following only the plastically deformed area on the left-hand side of the imprint is considered. The plastically deformed volume on the right-hand side of the indent is neglected, since a correct fabrication of cross-sections running exactly through the edge of the cube corner could not be ensured.

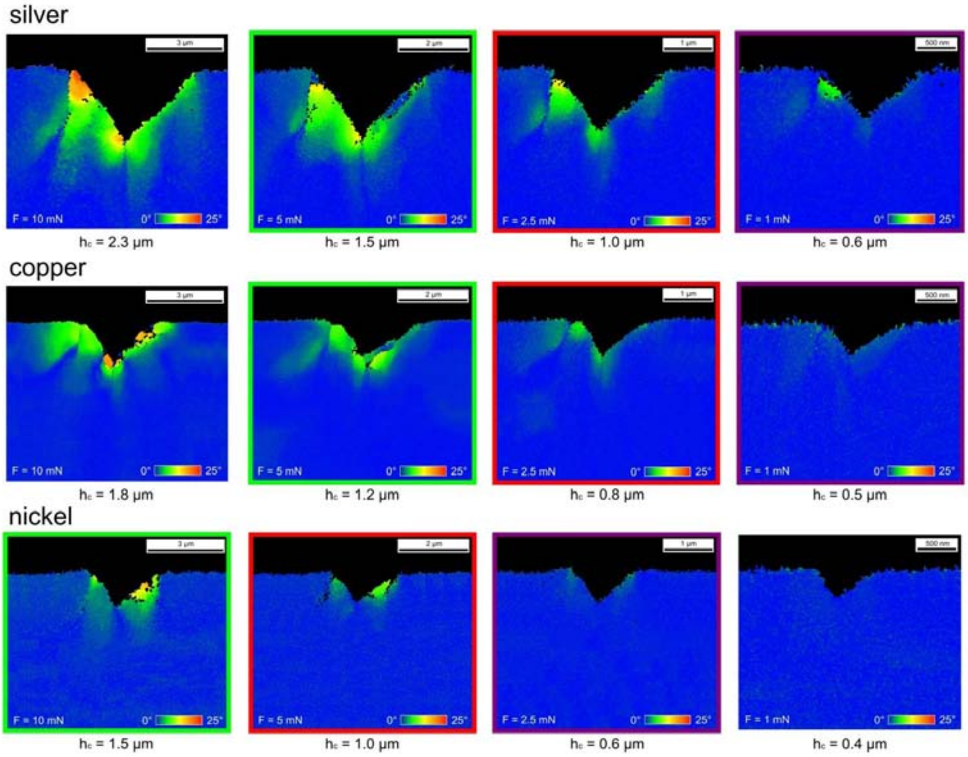

Figure E.5: Misorientation maps of cross-sections through imprints in silver, copper and nickel. For each material, loads of 10, 5, 2.5 and 1 mN, respectively, were used. Maps of imprints with approximately equal indentation depth are encircled by the same color (green: h_c = 1.2-1.5 μm, red: h_c = 0.8-1.0 μm, purple: h_c = 0.5-0.6 μm).

Figure E.5 presents the results of the EBSD study in terms of misorientation maps. Since all imprints were performed in load-controlled mode, indents in silver, copper and nickel exhibit different indentation depths. Therefore, only misorientation maps of imprints with similar indentation depth are compared. To make an interpretation of the results easier, maps representing indentations of similar depth are marked by the same color. Examining the misorientation maps of imprints with a depth between 1.2 and 1.5 μm (encircled green in Figure E.5), shows, for silver and nickel, deformation-induced patterns which are laterally strongly confined. For copper, however, the misoriented volume extends laterally to a distance of approximately two thirds of the imprint diameter. The axial extension of the misoriented zone for nickel shows a zone reaching deep into the bulk. In copper and silver, however, the zone has a somewhat smaller extension in this direction. Indentations with depths between 0.8 and 1 μm, those encircled red in Figure E.5, show a similar picture. As found for the deep imprints, the misoriented zone beneath the indents in nickel and silver is highly confined with an only small lateral extent. The deformation-induced pattern for copper, however, extends laterally to a distance equal to one-half of the imprint diameter. For imprints with depths between 0.5 and 0.6 μm (encircled purple in Figure E.5) the misoriented zone is only hard to detect. Due to the only minor crystal orientation changes caused by the small indentation depths, a useful interpretation of the misorientation maps is difficult.

However, significant differences between the misoriented zones of silver, copper and nickel, which can be attributed to the influence of the SFE, could not be observed. The deformation-induced patterns look very similar and show only slight differences between one other. In summary, it can be stated out that neither the investigations of the hardness curves, which is in agreement with that of Elmustafa and Stone,[21] nor the examinations of the cross-sections provide evidence that the SFE influences the ISE. A further interesting finding was that the reduced indentation modulus E_{red} normalizes the observed H vs. h curves rather well. However, to obtain more accurate information to explain the ISE, especially at very small indentation depths, transmission electron microscopy investigations of the deformation zone beneath imprints are absolutely essential.

Bibliography to paper E

[1] Seeger A. Z Naturforsch 1954;9a:856.

[2] Seeger A. Stacking faults in close-packed lattices. In: H H Wills Physical Laboratory University of Bristol, editor. Report of the Conference on Defects in Crystalline Solids. London: The Physical Society, 1955. p.328.

[3] Schoeck G, Seeger A. Activation energy problems associated with extended dislocations. In: H H Wills Physical Laboratory University of Bristol, editor. Report of the Conference on Defects in Crystalline Solids. London: The Physical Society, 1955. p.340.

[4] Swann PR, Nutting J. Inst Met 1961–62;90:133.

[5] Seeger A, Berner R, Wolf H. Z Phys 1959;155:247.

[6] Hirth JP, Lothe J. Theory of Dislocations. New York: Wiley; 1982.

[7] Kelchner CL, Plimpton SJ, Hamilton JC. Phys Rev B 1998;58:11085.

[8] Liang HY, Woo CH, Huang H, Ngan AHW, Yu TX. Philos Mag 2003;83:3609.

[9] Van Swygenhoven H, Derlet PM, Frøseth AG. Nat Mater 2004;3:399.

[10] Hasnaoui A, Derlet PM, Van Swygenhoven H. Acta Mater 2004;52:2251.

[11] Haasen P. Physikalische Metallkunde. Berlin: Springer; 1984.

[12] Landolt-Börnstein. Numerical Data and Functional Relationships in Science and Technology, Crystal and Solid State Physics, Vol. 2. Berlin: Springer; 1969.

[13] Vlassak JJ, Nix WD. Philos Mag A 1993;67:1045.

[14] Lyles Jr RL, Rothman SJ, Jäger W. Metallography 1978;11:361.

[15] Oliver WC, Pharr GM. J Mater Res 1992;7:1564.

[16] Rester M, Motz C, Pippan R. Acta Mater 2007;55:6427.

[17] Tabor D. Proc R Soc A 1947;192:247.

[18] Seeger A. Moderne Probleme der Metallphysik. Berlin: Springer; 1965.

[19] Gottstein G. Physikalische Grundlagen der Materialkunde. Berlin: Springer; 2001.

[20] Kiener D, Pippan R, Motz C, Kreuzer H. Acta Mater 2006;54:2801.

[21] Elmustafa AA, Stone DS. Mater Sci Eng A 2003;358:1.

F

Indentation across size scales – A survey of indentation-induced plastic zones in copper $\{111\}$ single crystals

M. Rester, C. Motz and R. Pippan

Erich Schmid Institute of Materials Science, Austrian Academy of Sciences,
A–8700 Leoben, Austria

Abstract

The indentation-induced plastic zones below indentations in copper $\{111\}$ single crystals, with depths ranging from 250 nm to 250 μm, were examined using electron backscatter diffraction technique. Analyzing the obtained orientation "micrographs" and the corresponding hardness plot, exhibits three clearly distinguishable regimes. Comparing the microstructure reflected in the identified regimes to the structure which evolves during the deformation of pure face-centered cubic single crystals, shows very good agreement.

Over a century yet, indentation technique has been used to measure the hardness of different materials.[1] Depending on the applied forces and consequently the obtained displacements, hardness measurement can be divided into macro-, micro- and nanoindentation. Macroindentation provides a quick and simple method to obtain the overall bulk hardness of a material and is thus often used in quality control. However, if it is required to identify e.g. the mechanical properties of individual phases or of thin films, macrohardness measurement is generally not the right method. Micro- and nanoindentation techniques, which apply only small loads are more appropriate for these tasks. In microindentation, typically pyramid-shaped Knoop or Vickers indenters are used for indentation testing. Dividing the applied load by the surface of the residual impression measured in a microscope, yields the hardness of the material. The typical length scale of the penetration depth is for microindentation in the order of microns. In nanoindentation tests, however, the applied loads and consequently the depth of indentations are further reduced.[2–4] As a result, a direct measurement of the residual impression is no longer possible. This problem can be solved using instrumented indentation testing (IIT), where the area of contact is determined by measuring the depth of penetration of the indenter into the specimen surface.[5] Due to this development, nanoindentation has become a major tool to investigate the mechanical properties of small scale volumes.

Comparing results of indentation tests at scales from a few hundreds of microns to a few nanometers shows, that the hardness increases with decreasing indentation depth. In particular, at the submicron scale the depth dependency of the hardness is highly pronounced. This phenomenon is indicated as indentation size effect (ISE) and is well known from numerous indentation studies.[6–11] In order to explain the observed ISE, great attempts are made to get insight into the indentation-induced deformation behavior. Particularly the implementation of focused ion beam (FIB) and electron backscatter diffraction (EBSD) techniques have facilitated a more accurate examination of the deformation zone beneath the imprint. Kiener et al.,[12] e.g., used conventional EBSD technology to investigate the deformed volume beneath Vickers indentations of depths between 2.4 μm and 700 nm. Zaafarani et al.,[13] on the other hand, applied 3D-EBSD technology to examine the texture and microstructure below a 900 nm deep spherical indentation. A similar study, but on a much larger imprint was performed by Kysar et al.,[14] who analyzed the crystal lattice rotations of an approximately 400 μm deep wedge indentation using a conventional EBSD device. Summing up the results of the already performed EBSD studies shows, that a wide range of indentation depths is covered. However, one matter which complicates a direct comparison of the results is the fact, that various indenter geometries, as well as different oriented single crystals were used in these experiments. In order to eliminate these restrictions and to ensure comparability, a survey across size scales of indentation-induced plastic zones below imprints of identical geometry, performed on equally oriented single crystals, would be of great interest.

In the present paper we report a study, where the microstructure beneath cube corner imprints from nanoindentations up to macroindentations is investigated. The covered penetration depth thereby reaches from 250 nm to 250 μm which correspond loads from 500 μN to 100 N. All indentations were performed on copper single crystals with an $\langle 1\bar{1}0 \rangle \{111\}$ orientation. The single crystals were all wet ground and mechanically polished, using alumina suspension with a grain size of 1 μm. Additionally the $\{111\}$ surface planes were electropolished to remove any deformation layer caused by mechanical polishing. In order to obtain a sharp edge, the plane perpendicular to the $\{111\}$ surface was subsequently carefully mechanically polished. Using three different indentation devices, several cube corner indentations were produced in the vicinity of the polished edge. The smallest indentations, those with loads of 0.5 mN, 1 mN and 10 mN were performed by means of a nanoindenter (Hysitron TriboScope), while for the 300 mN imprint an in-situ microindenter (ASMEC UNAT) was used. The largest indentations, with loads of 10 N and 100 N, respectively, were fabricated using a Kammrath & Weiss compression module. Cross-sections through the centre of all imprints were produced using a FIB workstation (LEO 1540 XB). Detailed information concerning the fabrication process and the used milling parameters can be found in.[15] Using a field emission SEM (LEO 1525) equipped with an EDAX electron backscatter diffraction system, EBSD investigations on the readily polished cross-sections were performed. Since plastic deformation causes changes of the crystal orientation, EBSD technique facilitates the visualization of traces of plastic deformation. The orientation changes were calculated using EBSD analysis software and visualized by means of color-coded misorientation maps.

Additionally to the indentations produced for cross-sectioning, several indentations were made from 40 μN to 100 N in order to determine the hardness of the material. Nanoindentations at loads between 40 μN and 10 mN were performed using a Hysitron Triboscope equipped with a cube corner indenter exhibiting a tip radius of about 40 nm. For every selected load three to five separate indentations were accomplished using a load-time sequence described in.[15] The plotted error bars in Figure F.1 and Figure F.3 represent the standard deviation of each set of measurements. The area function of the cube corner indenter was determined using the procedure outlined by Oliver and Pharr.[16] Indentations between 50 mN and 300 mN were accomplished by means of an ASMEC UNAT microindenter. The microindenter was fitted with a cube corner indenter and was operated in load controlled mode. Each load-time sequence consisted of 100 s loading to maximum load, 10 s holding at peak load, and 46 s unloading including a holding period of 20 s at 10% of the peak load. The material hardness was calculated dividing the applied force by the area of the residual impression determined by means of a LEO 1525 field emission SEM. Errors arising from sizing the imprint area in the SEM, are considered by the plotted error bars. Macroindentations were made in load-controlled mode with a Kammrath & Weiss compression module equipped with a cube corner indenter. Using a loading rate of 2.5 N/s and a holding period at peak load of 20 s, loads of 10 N, 50 N and 100 N respectively, were applied. Subsequently, the area of the residual imprints was measured and the hardness calculated. The plotted error bars consider errors which arise from determining the imprint area by means of a light microscope.

The results of the hardness measurement are presented in Figure F.1 (a), where a significant ISE can be observed. Starting with a value of 2.75 GPa at an indentation depth of 35 nm the hardness decreases to a value of approximately 0.6 GPa at a depth of about 250 μm. The arrows plotted in the diagram mark the hardness values of the examined indentations.

The corresponding EBSD misorientation maps performed on the fabricated cross-sections through the imprints are displayed in Figure F.2. The inset in Figure F.2 (f) shows the position of the imprints with respect to the crystallographic orientation of the single crystal. Since the surface normal of the copper crystal is of type [111] and the crystallographic direction parallel to the investigated surface is of type $[1\bar{1}0]$, the direction normal to the cross-sections is $\langle 11\bar{2} \rangle$. The azimuthally orientation of the cube corner indenter was chosen in that way, to have one side of the impression parallel to the $\langle 11\bar{2} \rangle$ direction. Furthermore it has to be noticed, that in the following only the left-hand part of the deformation zone is considered, since correct sectioning on the right-hand side, through the imprints edge, can not be ensured. Starting with the misorientation maps of the smallest sectioned indentations, those made at loads of 0.5 mN and 1 mN (Figure F.2 (a) and (b)), show the formation of patterns consisting of two characteristic sections. As demonstrated in a former work[15] section I and II are rotated contrary and are separated by a less pronounced arrangement of dislocations. Noticeable is the relatively large lateral extension of section I, as well as the ambiguous character of both sections. This is due to the fact that the misorientation patterns are built up by only few dislocations.[17] Increasing the load and as a consequence the penetration depth yields to a significant increase of the misorientation and to the formation of strongly pronounced patterns (see 10 mN indent in Figure F.2). As can be seen, a third characteristic section denoted III which rotates contrary to section II, appears.[15] Additionally it has to be noticed, that in the misorientation maps of the large imprints a less sensitive color code was used. Compared to the highly ambiguous patterns of the 0.5 mN and 1 mN imprints, the misorientation patterns of the 10 mN indent look well defined. Analyzing the patterns in the TEM shows for the 10 mN indentation a deformation zone built up by structures of high dislocation density, while the deformation zone of the 0.5 mN indentation consists of only few dislocation loops.[17] It seems that the single dislocations which surround the shallow imprint and induce the observed only slight misorientation gradients, are responsible for the ambiguous character of the deformation patterns. The misorientation map of the 300 mN indentation (Figure F.2 (d)) shows similarity to the 10 mN imprint. Here as well three sections, which characterize the traces of deformation, appear. Differences to the 10 mN imprint can be found in a much more confined section II and in a vertical line below the imprints tip, associated with the already known change of the shear stress field. Figure F.2 (e) represents the misorientation map of a 10 N imprint. Investigating the map, shows that only two characteristic sections appear. Interesting is the high axial and an only minor lateral extension of section I. Section II, on the other hand, is axially more limited. As can be seen, the deformation pattern in section II is axially extended by slip bands which are symmetrically arranged at the centerline. Laterally,

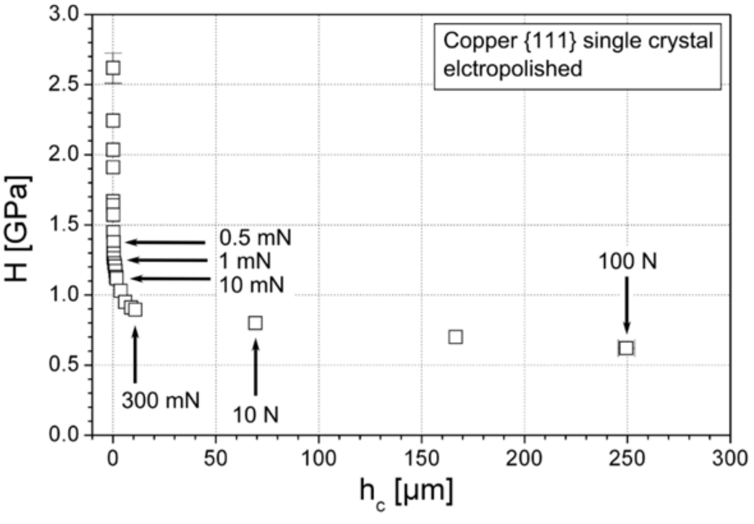

(a)

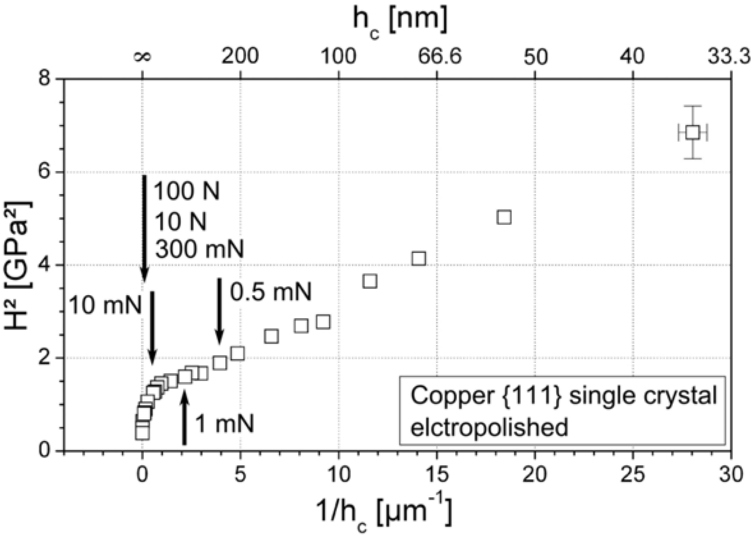

(b)

Figure F.1: (a) Hardness as a function of indentation depth and (b) square of the hardness as a function of the reciprocal indentation depth, for loads ranging from 40 μN to 100 N. The arrows mark the hardness values of imprints investigated in course of this work. Error bars are inserted only for those datum points where the error bar is larger than the size of the symbol.

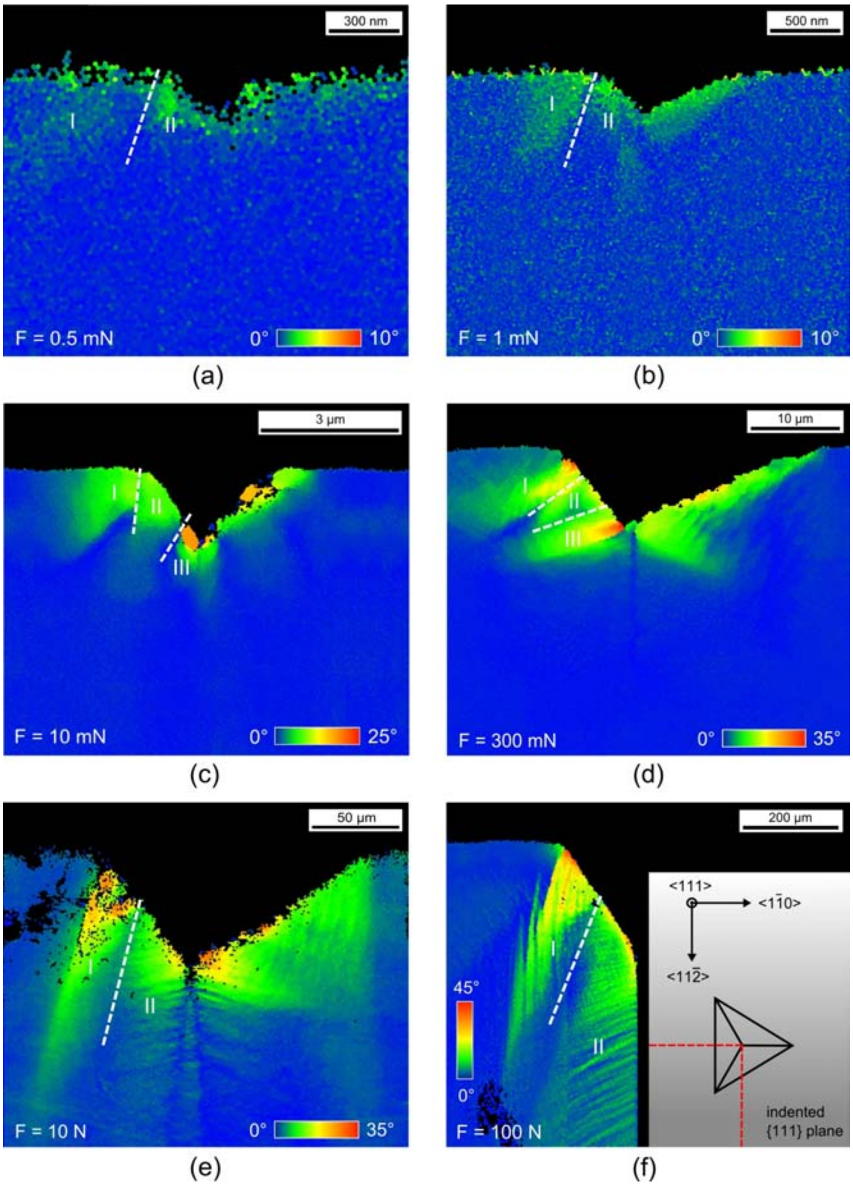

Figure F.2: Misorientation maps of indentations in copper for loads of 0.5 mN, 1 mN, 10 mN, 300 mN, 10 N and 100 N. The maps (a)–(e) represent the whole cross-section of the indentations, while for the 100 N indentation only one half of the cross-section is displayed. Noticeable is that in the misorientation maps different color codes have been used. The inset in (f) shows the position of the imprints with respect to the crystal orientation as well as how the 100 N indentation was cut.

section II is enclosed by the changing shear stress field on the right-hand side, and by the deformation pattern of section I on the left-hand side. The deformation-induced zone of the largest investigated indentation, performed at a load of 100 N, is displayed in Figure F.2 (f). Mentionable is, that only the left-hand side of the imprint was cross-sectioned, in order to keep the FIB milling time down. As already found for the 10 N indentation, here as well the deformation-induced zone consists of two characteristic sections. Both sections are laterally strongly confined, while axially they reach far into the bulk. Noticeable is the strong fragmentation of the deformation pattern into substructures.

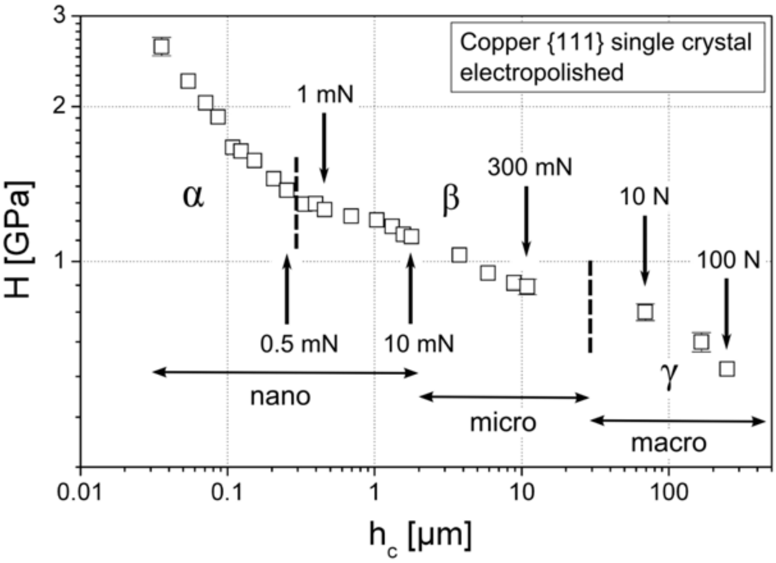

Figure F.3: Logarithmic plot of the hardness versus the indentation depth for loads ranging from 40 μN to 100 N. The arrows mark the hardness values of imprints investigated in course of this work. Error bars are inserted only for those datum points where the error bar is larger than the size of the symbol.

It has to be mentioned that the described changes in the evolution of the microstructure are not reflected in the hardness curves presented in Figure F.1, neither in the H vs. h_c plot (a) nor in the H^2 vs. $1/h_c$ plot (b). However, replotting the data in a logarithmic diagram shows three clearly distinguishable regimes (see Figure F.3). Comparing the identified regimes denoted by α, β and γ , to the different "structure-formation" processes found in Figure F.2, show very good agreement. In regime α, where the imprints are smaller than approximately 200 nm, no significant orientation changes were detected (cp. Figure F.2 (a)). Regime β, which describes indentations between 200 nm and 10 μm in depth, is characterized by regions exhibiting distinctive changes of the orientation (cp. Figure F.2 (c) and (d)). Noticeable is, that in this regime the dimension of the misorientation patterns are proportional to the size of the imprint. Furthermore, the orientation differences increases with growing indentation depth, especially between 200 nm and 1 μm. Regime γ, on the other hand, associated with indentations larger than 10 μm, is indicated by a substructure which typically forms during the deformation of face-centered cubic (fcc) single crystals of pure metals (cp. Figure F.2 (e) and (f)). In order to facilitate the subsequent discussion, in the following the salient fundamental features of strain hardening behavior of single crystals are listed:

- The hardening behavior of a single crystal shows different stages, denoted I, II, III, IV and V.
- The onset-stress for plastic deformation of fcc single crystals of pure metals is very low and their flow stress exhibits an extraordinary high hardening capacity.
- The dislocation structure developed in a single crystal depends significantly on the applied strain and the path the straining is accomplished. It usually starts by the formation of micro- and macro slip bands and proceeds by the generation of cells and cell block structures. Further deforming, keeps the process of fragmentation on. Finally, at very large strains a saturation structure with a minimum crystallite size is reached. For copper single crystals deformed at room temperature, this crystallite size is in the order of a few 100 nm.[18]
- Additionally it has to be considered, that in case the imprint size is significantly larger than the dimension of the deformation-controlling microstructure, the hardness should be independent of the imprint size.

Keeping the aforementioned facts in mind, it becomes evident that the size of the investigated imprints covers a wide range of the different scales of structural evolution, which occur during the deformation of a single crystal. Due to these facts it is not surprising that hardness changes with the size of indentation. As can be seen, regime α is characterized by an imprint size, which is lower than the smallest structural element of a single crystal deformed at very large strains. At such small imprints, no substructure exhibiting large misorientation gradients, is generated. It is assumed that the indentation is realized by dislocation loops, pushed into the crystal, building up a “prismatic loop”-like structure. Since the loops arrange in a very wide spread manner, the resulting orientation changes are only small.[17,19] In this regime, plastic flow is controlled by the source stress and the back stress of already existing dislocations. Regime β is characterized by substructures, which are typical for heavy plastically deformed single crystals. The dimensions of these structures are dependent on imprint size and the amount of misorientation between the different regions. As demonstrated in Figure F.2, augmentation of the indent size yields to an increased size of the substructure. It seems that the increasing substructure size is responsible for the decreasing hardness, similar to the observed decrease of flow stress with increasing grain size. The characteristic of regime γ, are regions with a substructure similar to low and medium deformed single crystals. It can be seen from Figure F.2 (e) and (f) that these regions, which exhibit a structure that typical develops at lower strains, become more and more important. This already known fact,[20] seems to be responsible for a further reduction of the hardness.

In the authors opinion the very low stress necessary for the onset of plasticity in pure fcc metals, the very high hardening capacity and the formation of different substructures causes the ISE for the relatively large imprints. Summarizing, the following conclusions can be drawn: The hardness of a material varies with the size of the indent, as the flow stress of a single crystal with the evolving substructure. Only for very small imprints (i.e. in regime α), the source size becomes the dominant effect.

Bibliography to paper F

[1] Tabor D. The Hardness of Metals. Oxford: Clarendon Press; 1951.

[2] Pethica JB, Hutchings R, Oliver WC. Philos Mag A 1983;48593.

[3] Doerner MF, Nix WD. J Mater Res 1984;1:601.

[4] Oliver WC, Hutchings R, Pethica JB. Measurements of hardness at indentation depths as low as 20 nanometers. In: Blau PJ, Lawn BR, editors. Microindentation Techniques in Materials Science and Engineering, Spec. Tech. Publ. 889. Philadelphia: American Society of Testing and Materials, 1986. p.90.

[5] Fischer-Cripps AC. Nanoindentation. New York: Springer; 2004.

[6] Nix WD, Gao H. J Mech Phys Solids 1998;46:411.

[7] Gane N, Cox JM. Philos Mag 1970;22:881.

[8] Ma Q, Clark DR. J Mater Res 1995;10:853.

[9] Stelmashenko NA, Walls MG, Brown LM, Milman YV. Acta Metall Mater 1993;41:2855.

[10] McElhaney KW, Vlassak JJ, Nix WD. J Mater Res 1998;13:1300.

[11] Lim YY, Chaudhri MM. Philos Mag A 1999;79:2979.

[12] Kiener D, Pippan R, Motz C, Kreuzer H. Acta Mater 2006;54:2801.

[13] Zaafarani N, Raabe D, Singh RN, Roters F, Zaefferer S. Acta Mater 2006;54:1863.

[14] Kysar JW, Gan YX, Morse TL, Chen X, Jones ME. J Mech Phys Solids 2007;55:1554.

[15] Rester M, Motz C, Pippan R. Acta Mater 2007;55:6427.

[16] Oliver WC, Pharr GM. J Mater Res 1992;7:1564.

[17] Rester M, Motz C, Pippan R. Mater Res Soc Symp Proc 2007;1049:AA03-03.

[18] Hafok M, Vorhauer A, Keckes J, Pippan R. Mater Sci Forum 2006;503–504:621.

[19] Balint DS, Deshpande VS, Needleman A, Van der Giessen E. J Mech Phys Solids 2006;5:2281.

[20] Schulz F, Hanemann H. Z Metallk 1941;33:124.

G

TEM sample preparation using the FIB lift-out method and low energy ion milling

M. Rester

Erich Schmid Institute of Materials Science, Austrian Academy of Sciences,
A–8700 Leoben, Austria

Abstract

The use of focused ion beam (FIB) milling for the preparation of site-specific transmission electron microscopy (TEM) samples is very important for material science. Usually, ions with a kinetic energy of approximately 30 keV are used for thinning specimens to electron-transparency. The results are damage structures on the sample surface, which makes a detection of pre-existing defects very difficult, or even impossible. In the following we present a method to prepare damage minimized site-specific TEM specimens by means of FIB low energy milling. Additionally, the sample made with FIB low energy milling is compared to a specimen prepared with FIB high energy milling.

G.1 Introduction

In recent years, focused ion beam (FIB) technique has become the method of choice to prepare site-specific transmission electron microscopy (TEM) samples.[1] The so-called in-situ lift-out technique, which was first proposed by Overwijk et al.[2] and further developed by Giannuzzi et al.,[3] is thereby the most used method to directly remove electron-transparent thin foils from a bulk specimen. For thinning of the foils, typically ion beams accelerated by 30 kV are used, which results in massive damage of the the specimen surface. The consequences are gallium contaminations, the amorphization of the surface and/or the formation of defect agglomerates and intermetallic phases.[4–15] Due to the extensive microstructural modifications of the sample, the analysis of pre-existing defects is massively impeded. Minimization of damage can be achieved by two ways: 1) Reducing the incidence angle of the impinging Ga^+ ions and 2) using lower ion energies.[16] Since the ion beam is parallel to the surface to be thinned, reduction of the incidence angle is no option. Consequently, the acceleration voltage of the Ga^+ ions has to be reduced. In the following we report on the use of a low energy module attached to a LEO 1540 XB FIB workstation, to fabricate damage-minimized TEM samples. The fabrication process is explained by means of manufacturing a cross-sectional TEM sample through the center of a nanoindentation. Special attention is paid to give a detailed description of the steps, necessary to produce low-energy thinned specimens.

G.2 Specimen preparation method

Copper {111} single crystals were prepared by wet grinding and mechanical polishing. Subsequently the {111} surface was electropolished, in order to remove any deformation layer produced during prior polishing steps. Using a Hysitron TriboScope fitted with a cube corner indenter, indentations with loads of 10, 2.5 and 1 mN, respectively, were performed on the readily polished surface. By means of a LEO 1540 XB focused ion beam (FIB) workstation, cross-sectional TEM samples were fabricated. For this purpose, the center of the imprint was marked and a protection layer was deposited.[17] The protection layer should exhibit a thickness of about 1–2 μm. Subsequently to deposition, two trenches on each side of the imprint were cut, which resulted in an approximately 2 μm thick foil containing the indentation. By means of a micromanipulator the foil was lifted out and fixed to a TEM sample holder. A series of images showing the lift-out process is presented in Figure G.1. More detailed information on in-situ sample lift-out can be found in the work of Massl.[18] The description given in the following starts, where the lifted out foil is already fixed to the TEM sample holder.

Using an acceleration voltage of 30 kV and an ion current of 500 pA, the foil is thinned coarsely. For this purpose, the sample has to be tilted to approximately 55.2°. Due to the convergence of the beam, "over-tilting" is necessary in order to obtain an equally thinned sample. Subsequently, the sample holder is rotated by

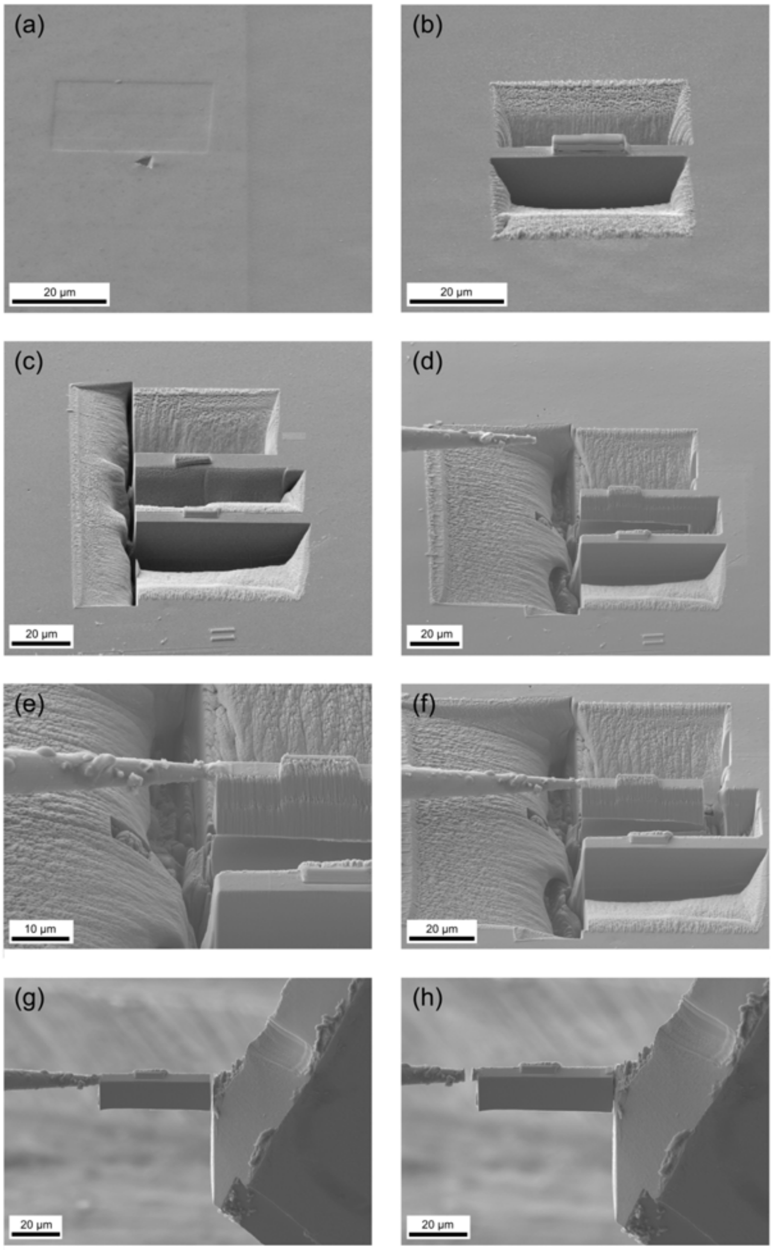

Figure G.1: Series of images showing the lift-out process of a foil. (a) Indent on a {111} surface of a copper single crystal. (b) Indent covered by a protection layer and cut free by two trenches. (c)–(d) Free cutting of the foil and positioning of the micromanipulator needle. (e) Using the gas injection system (GIS) to mount the micromanipulator needle to the foil. (f) Free cutting and lift-out of the foil. (g) Positioning of the foil to the TEM specimen holder. (h) Using the GIS to mount the foil to the TEM specimen holder.

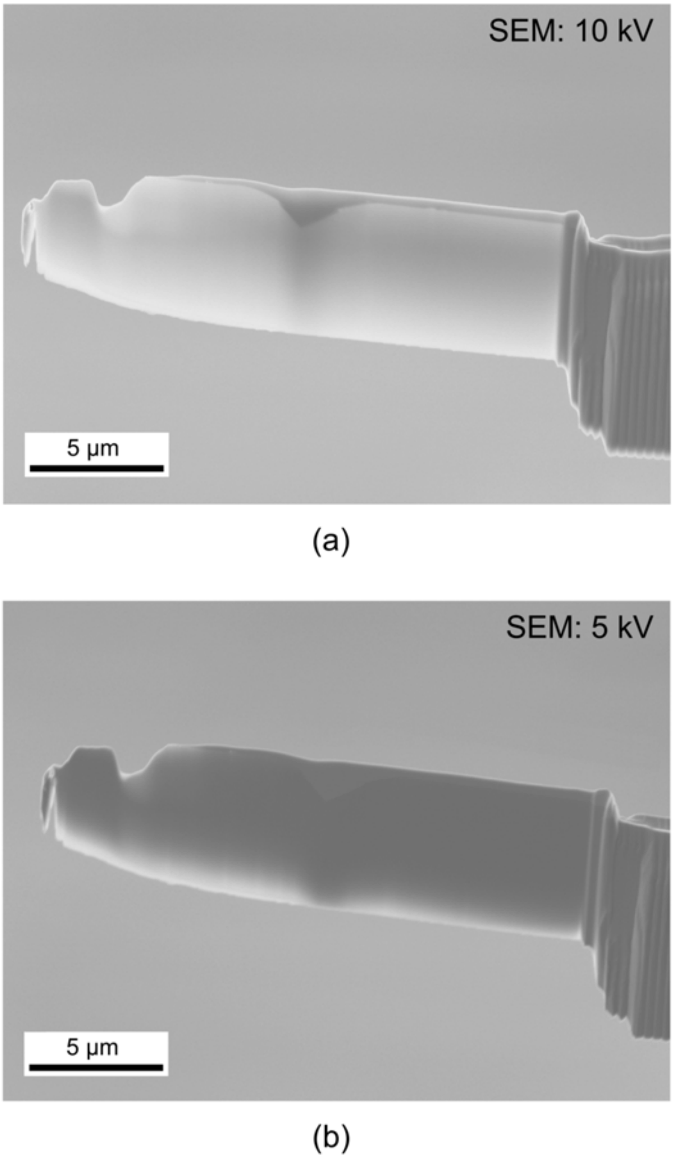

Figure G.2: SEM micrographs of an unfinished TEM foil taken at (a) 10 kV and (b) 5 kV acceleration voltage in SEM high current mode.

180° to enable polishing of the back side. Thinning of the back side is as long performed as the sample starts to get transparent in SEM mode at 10 kV (see Figure G.2 (a)). Changing the SEM acceleration voltage to 5 kV, yields to a picture similar to those shown in Figure G.2 (b). In a next step, the ion gun is switched into low energy mode; for that reason shutting down of the gun is required. After setting the acceleration voltage to 5 kV, the gun can be restarted. As Figure G.3 (b) demonstrates, reducing the acceleration voltage results in a poor resolution of FIB imaging. Since the convergence of the beam is further increased by reducing the ion energy, the sample has to be tilted to 60.5°. Also included in Figure G.3 (b) is a sketch, showing how the milling rectangle should be positioned. Selecting a milling current of 200 pA and a time period of 600 s, the milling job can be executed. During milling an accurate observation of the foil is essential in order to prevent unequal material removal. In case of irregular removal the tilting angle of the specimen has to be corrected. After finishing the front side and rotating the sample by 180°, milling of the back side can be started. The thinning process is completed when the foil gets electron-transparent in SEM mode at 5 kV.

The subsequently accomplished TEM analyses, were performed using a Philips CM12 transmission electron microscope operating at an acceleration voltage of 120 kV.

G.3 Results and discussion

A cross-sectional bright-field TEM image of a 1 mN indentation, prepared in low energy milling mode, is presented in Figure G.4 (a). For comparison a TEM image of a 2.5 mN indent, thinned with an acceleration voltage of 30 kV, is shown in Figure G.4 (b). It is apparent from both micrographs that the sample thinned with higher energy (Figure G.4 (b)) exhibits a much more damaged surface. The damage structure possess a strain contrast, comparable to a dislocation network imaged under two beam condition. Consequently, the detection of pre-existing artifacts is impeded or even impossible. The low energy sample, on the other hand, shows only slight damage of the surface. However, avoiding the formation of defects completely, seems to be impossible. A more detailed description on FIB damage, especially for copper, can be found in the work of Kiener et al.[15]

G.4 Conclusions

Summarizing it can be said, that low energy FIB technology minimizes the damage considerably, however, the preparation of artifact-free TEM samples is up to now not possible. Due to this fact, FIB low energy milling is essential to fabricate damage-minimized TEM specimens.

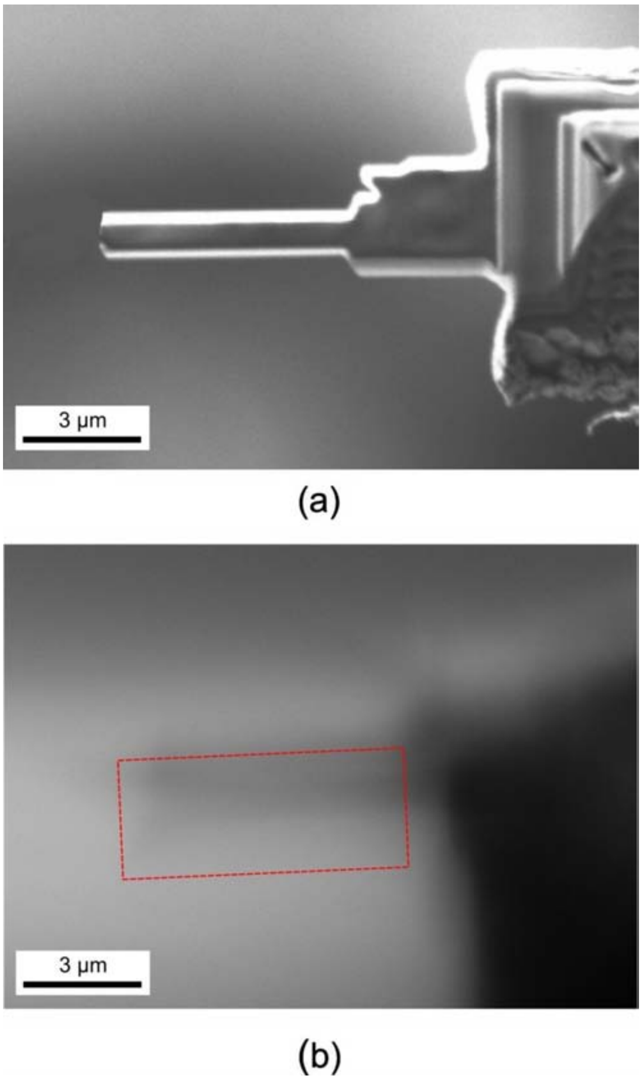

Figure G.3: FIB micrographs of an unfinished TEM foil taken at an acceleration voltage of (a) 30 kV and (b) 5 kV. The ion current in both cases was 200 pA. The rectangle in (b) shows, how the milling window should be positioned.

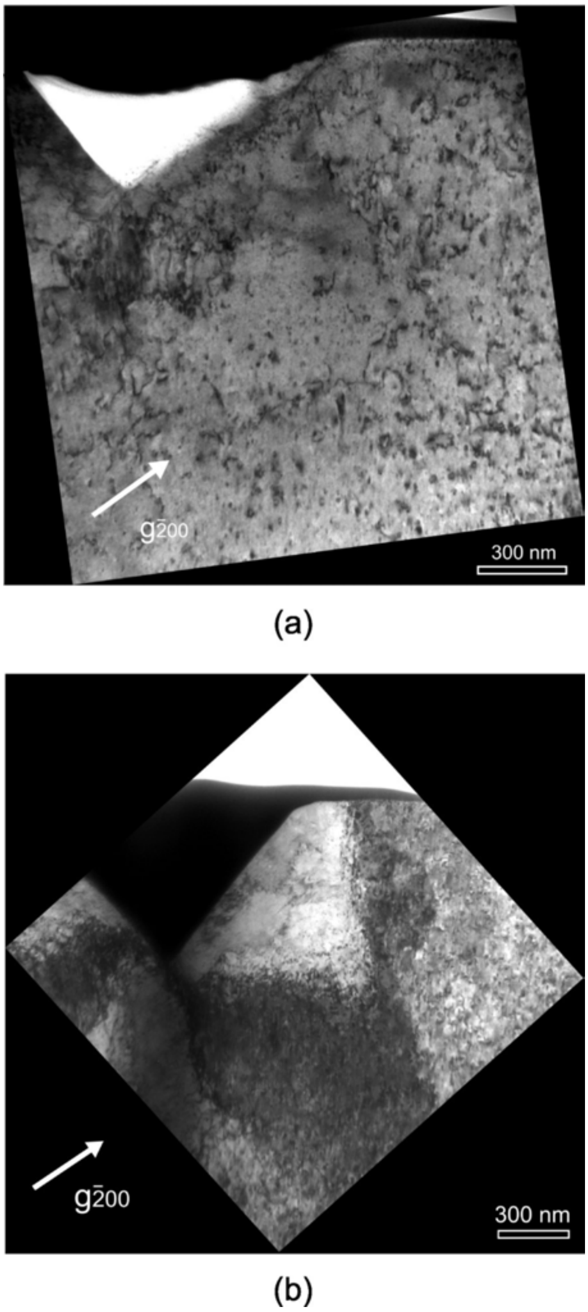

Figure G.4: Cross-sectional TEM micrographs through the center of indentations made at loads of 1 mN (a) and 2.5 mN (b), respectively. The thin foil presented in (a) was prepared with gracing incident Ga^+ ions with a kinetic energy of 5 keV, while for (b) ions with a kinetic energy of 30 keV were used. Both micrographs were taken with a $\bar{2}00$ two beam condition.

Bibliography to paper G

[1] Giannuzzi LA, Stevie FA. Introduction to Focused Ion Beams: Instrumentation, Theory, Techniques, and Practice. New York: Springer; 2005.

[2] Overwijk MHF, van den Heuvel FC, Bull-Lieuwma CWT. J Vac Sci Technol B 1993;11:2021.

[3] Giannuzzi LA, Stevie FA. Micron 1999;30:197.

[4] Marien J, Plitzko JM, Spolenak R, Keller RM, Mayer J. J Microsc 1999;194:71.

[5] Larson DJ, Foord DT, Petford-Long AK, Liew H, Blamire MG, Cerezo A, Smith GDW. Ultramicroscopy 1999;79:287.

[6] Jamison RB, Mardinly AJ, Susnitzky DW, Gronsky R. Microsc Microanal 2000;6:526.

[7] Rubanov S, Munroe PR. J Mater Sci Lett 2001;20:1181.

[8] McCaffrey JP, Phaneuf MW, Madsen LD. Ultramicroscopy 2001;87:97.

[9] Rubanov S, Munroe PR. Mater Lett 2003;57:2238.

[10] Prenitzer BI, Urbanik-Shannon CA, Giannuzzi LA, Brown SR, Irwin RB, Shofner TL, Stevie FA. Microsc Micronanal 2003;9:216.

[11] Hutchinson CR, Hackenberg RE, Shiflet GJ. Ultramicroscopy 2003;94:37.

[12] Rubanov S, Munroe PR. J Microsc 2003;214:213.

[13] Wang Z, Kato T, Hirayama T, Sasaki K, Saka H. Appl Surf Sci 2005;241:80.

[14] Yu J, Liu J, Zhang J, Wu J. Mater Lett 2006;60:206.

[15] Kiener D, Motz C, Rester M, Jenko M, Dehm G. Mater Sci Eng A 2007;459:262.

[16] Scott J, Docherty FT, MacKenzie M, Smith W, Miller B, Collins CL, Craven AJ. J Phys Conf Series 2006;26:223.

[17] Rester M, Motz C, Pippan R. Acta Mater 2007;55:6427.

[18] Massl S. Investigation of Deformation Structures Resulting from Semi-Brittle Fracture in Recrystallized Tungsten and High Nb-Containing Two-Phase TiAl. Leoben: University of Leoben; 2005.